

Star Formation History and Other Properties of the Northern HDF

Rodger I. Thompson

Steward Observatory, University of Arizona, Tucson, AZ 85721

ABSTRACT

The original analysis of the star formation history in the NICMOS Deep images of the NHDF is extended to the entire NHDF utilizing NICMOS and WFPC2 archival data. The roughly constant star formation rate from redshifts 1 to 6 found in this study is consistent with the original results. Star formation rates from this study, Lyman break galaxies and sub-mm observations are now in concordance. The spike of star formation at redshift 2 due to 2 ULIRGs in the small Deep NICMOS field is smoothed out in the larger area results presented here. The larger source base of this study allows comparison with predictions from hierarchical galaxy formation models. In general the observations are consistent with the predictions. The observed luminosity functions at redshifts 1-6 are presented for future comparisons with theoretical galaxy evolution calculations. Mid and far infrared properties of the sources are also calculated and compared with observations. A candidate for the VLA source VLA 3651+1221 is discussed.

Subject headings: Early Universe — galaxies:evolution — galaxies:distances and redshifts

1. Introduction

The Hubble Deep Fields (HDFs) are rich sources of data on cosmology and the evolution of galaxies. The large number of observations at many different wavelengths make the Northern HDF (NHDF) particularly useful. The NHDF is the only HDF that has complete coverage with both WFPC2 and NICMOS. The NICMOS coverage, however, is not to the same depth as the WFPC2 due to the smaller area of the NICMOS Camera 3. This is somewhat compensated for by the red nature of evolved galaxies and the redshift of visible light into the infrared bands for young blue galaxies.

This work studies the star formation history in the NHDF and is an extension of a similar study utilizing the smaller NICMOS Deep field (Thompson, Weymann and Storrie-Lombardi 2001) (hereinafter TWS). The increased area and number of galaxies greatly improves the statistical significance of the results over TWS. Shallower coverage, however, increases the photometric error, making it comparable or dominant over the large scale structure error which decreased due to the larger field.

Other researchers, Lanzetta, Yahil & Fernández-Soto (1996); Fernández-Soto, Lanzetta, & Yahil (1999); Lanzetta et al. (2002) have utilized the same data set, plus additional ground based data to investigate star formation history in the NHDF. Our analysis differs significantly from those studies by including extinction in the SED templates used to determine the photometric redshifts. This produces results quite different from Lanzetta et al. (2002) who do not include extinction. Contrary to Lanzetta et al. (2002) we find that the star formation rate (SFR) is essentially constant in the epoch from $z = 1$ to $z = 6$ and that this rate is significantly larger than the present day SFR (Lilly et al. 1996), consistent with the results presented in TWS.

2. Observations

Observations utilized in this study are all from the Hubble Space Telescope (HST) archives. The first set is the processed WFPC2 images of the NHDF produced by Williams et al. (1996). The second set is the archival data from the NICMOS survey of the entire NHDF by Dickinson (2000). The NICMOS F110W and F160W data were reprocessed as described in § 3. Only the areas corresponding to the three wide field WFPC2 chips are used since the WFPC2 PC chip images have substantially different signal to noise statistics. NICMOS Deep NHDF images and data reductions from Thompson et al. (1999) and TWS are used in the error analysis.

All NICMOS images were taken in the SPARSE64 mode with 24 samples after the first read and integration times of 1344 seconds. Images at 8 positions completely covered the NHDF. At each position 9 images were taken in a dithered pattern. The 8 positions with 9 dither points in the F110W and F160W filters required 144 exposures.

3. Data Reduction

The data reduction procedures are almost identical to the procedures described in Thompson et al. (1999) and TWS. For this reason they will only be briefly outlined except

where there are differences. The WFPC2 images were not altered from the Version 2 images available in the HST archives. The NICMOS images, however, were reduced from the raw images obtained in the HST cycle 7 program 7817 by Mark Dickinson. The images were examined for effects of cosmic ray persistence from SAA passages and 17 of the 144 images were rejected. The background flux was removed by taking the median of the images in each filter that were not affected by cosmic ray persistence and subtracting it from each image.

The 9 dithered images for each of the 8 positions were combined using the standard Drizzle procedures with 0.1 arc second pixels, one half the linear size of the NICMOS Camera 3 pixels. The IDL procedure IDP3 (Lytle et al. 1999) produced a mosaic of the 8 images. IDP3 also reduced the WFPC images to the NICMOS resolution with a bi-cubic spline interpolation and aligned them with the NICMOS mosaic. Inspection of the images showed regions of increased noise at the boundaries between images. These areas were masked out as shown in Figure 1. Since this study is primarily a statistical study, the small amount of masked area does not affect the conclusions.

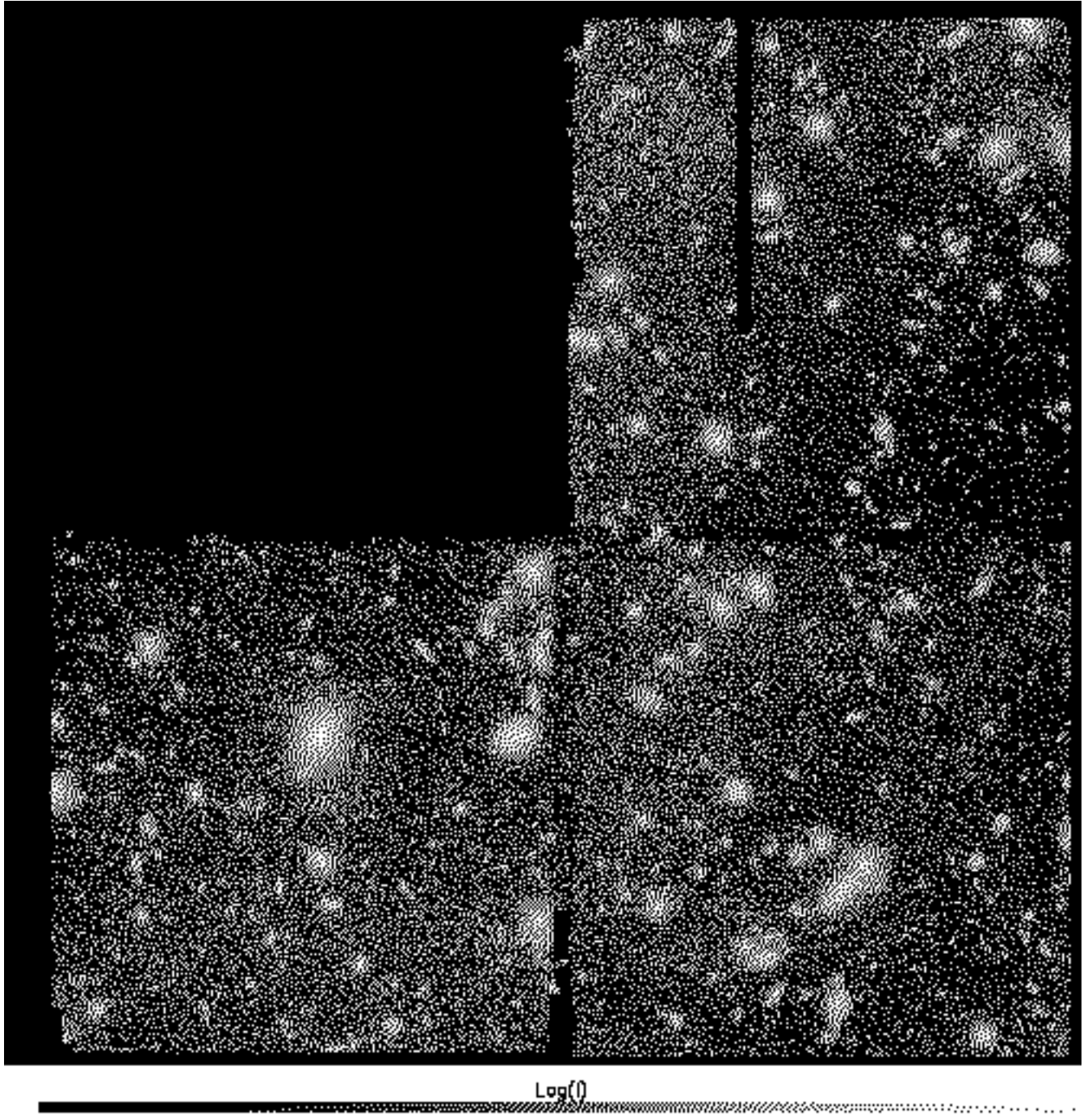


Fig. 1.— The masked areas shown on the WFPC2 F814W filter image of the NHDF.

Source positions were found using the method of Szalay, Connolly, & Szokoly (1999) as described in TWS. A Gaussian fit to the histogram of pixel values determined the global variance of the image mosaic in each filter. The histogram is dominated by the background noise with true sources creating a deviation from the Gaussian fit at large positive values. The 1σ noise levels in both the F110W and F160W NICMOS filters are 5×10^{-4} ADUs per second. For comparison the NICMOS Deep Field has a 1σ noise level of 2.2×10^{-4} ADUs per second. 5×10^{-4} ADUs per second corresponds to 1.4×10^{-9} Janskys. The drizzling procedure, however, introduces correlation, therefore, the true noise level is about 1.6 times larger than the measured Gaussian noise.

The Szalay source identification procedure requires images with a local variance of one. The local variances for the F110W and F160W fields were found by drizzling and mosaicing the flat fields of the two filters in exactly the same way as the images. This accounts for differences in sensitivity over the area of the NICMOS Camera 3 detector. The flats have a median of 1, therefore, the variance images also have a median of 1. The ratio of the imaged fields to the variance image was scaled to the average variance creating a local variance of 1. The variance in the WFPC filters was assumed constant across the field. This procedure differs slightly from the procedure used in TWS.

The threshold value of the Szalay R parameter, $\sqrt{\chi}$, was set to 4.5, higher than the 2.3 value used in TWS but more appropriate for the six dimensional χ^2 analysis of the combined WFPC and NICMOS fluxes. Unlike TWS all six fluxes are included in the Szalay procedure to insure that small blue galaxies with little infrared flux are not missed in the source extraction. The source selection criterion for determining the star formation history (§ 5.1), however, does discriminate against galaxies with no F110W or F160W flux. Figure 2 shows the distribution of R image pixels. All pixels with R values higher than or equal to 4.5 are considered legitimate source pixels. Pixels with R values less than 4.5 are assigned random values with average values 10^6 below the valid pixels. This forces the source extraction program to only consider pixels chosen by the Szalay procedure. The source extraction program crashes if all non-valid pixels are set to zero.

The source extraction program SExtractor (SE) (Bertin and Arnouts 1996) extracts the sources in two passes. The first pass on the R has the extraction threshold set at 4.0, selecting all valid pixels. As in TWS the DETECT MINAREA parameter is set to 3 so a true source must have 3 contiguous valid pixels. The source positions, except for the contiguous area criterion are, therefore, determined by the Szalay procedure, *not by SE*. SE then runs again on the six photometric images in a mode that extracts sources in the pixel pattern determined by the first pass. Run in this manner, SE does not produce daughter objects. Sources which have several components may be broken into individual objects by this process.

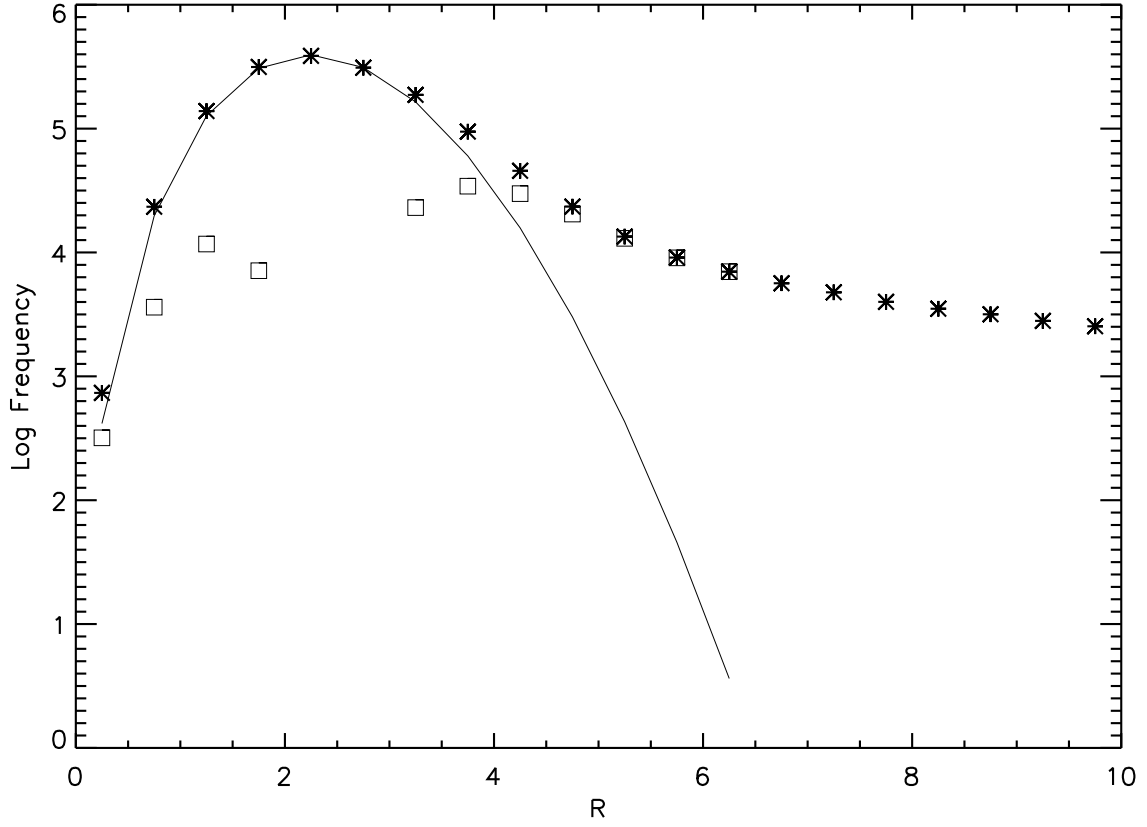


Fig. 2.— R image pixel distribution from the Szalay procedure. The asterisks represent the actual data and the solid line is the expected χ^2 distribution with six degrees of freedom. The boxes show the difference between the data minus the expected distribution. The long tail at high R is the real source distribution.

Although listed as separate objects in the catalog the star formation history is unaffected as long as the calculated photometric redshift is the same for both components. In some cases a separate listing for two components is an advantage, allowing different extinctions for different components. § 5.1 discusses additional criteria for final source selection.

The PHOT-APERTURES parameter in the SE configuration file was set to 6, 10, 15 to produce 0.6'', 1.0'', and 1.5'' diameter aperture fluxes. The photometric, redshift, extinction and SED calculations use the 0.6'' aperture fluxes. The total flux for determining the SFR is found by summing all of the pixels identified by the Szalay procedure as belonging to a single source.

4. Photometric Redshift, Extinction and SED Determination

The basic procedure for photometric redshift, extinction and SED determination is a χ^2 comparison of the observed fluxes in the six bands to fluxes calculated from numerically redshifted and extinguished SEDs. As described in TWS we draw our templates from three sources. The first source is the four observed SEDs of Coleman, Wu, and Weedman (1980) utilized by several authors. These galaxy SEDs have been corrected for galactic extinction but not for extinction in the galaxies themselves. The galaxies, however, were selected on the basis of their very low internal extinction. The unreddened SED of the set of mean SEDs of Calzetti, Kinney & Storchi-Bergmann (1994) provides an additional observed active star-forming galaxy template (Calzetti (1999a)). A final and even hotter template is a 50 million year old continuous star formation SED calculated from the Bruzual and Charlot models (Bruzual and Charlot (1996)) with a Salpeter IMF and solar metallicity. This theoretical SED does not have emission lines, therefore we have added H α , (O[III]+ H β) and O[II] emission lines by scaling up the lines from the Calzetti SED by the ratio of the UV fluxes in the Calzetti and Bruzual–Charlot SEDs. Template 6 is substantially bluer than the Calzetti SED.

Extinction is calculated from the starburst and star forming galaxy optimized obscuration law of Calzetti, Kinney & Storchi-Bergmann (1994). Since the primary purpose of this paper is a determination of the star formation rate it is appropriate to utilize an extinction law determined from star forming galaxies. The absorption due to extragalactic neutral hydrogen is calculated from an updated version of the formulation of Madau et al. (1996). The calculated fluxes are then interpolated between the 6 SEDs to produce 51 different SED fluxes for each redshift and extinction point. The details of this procedure are given in TWS. The grid for the χ^2 analysis includes 100 different redshifts between 0 and 8, 15 different extinctions between E(B-V) of 0 to 1.0 and 51 different interpolated template types for a

total of 7.65×10^4 choices. The resulting redshifts, extinctions and SEDs are given in Table 2. The earliest SED has a value of 1.0 incremented by 0.1 to the latest SED of 6.0. Integer values refer to the 6 basic SED templates. Extinctions in E(B-V) are incremented by 0.02 from 0 to 0.1 and by .1 from 0.1 to 1.0, the maximum used in the analysis.

The χ^2 procedure is identical to TWS except that negative fluxes are not replaced by zero. The technique minimizes the χ^2 residuals between the observed fluxes and those predicted by the numerically redshifted, extinguished and Lyman absorption attenuated SEDs. It alters the usual error term in the denominator by adding a second term proportional to the measured flux. The χ^2 residual is

$$\chi(z, E)^2 = \sum_{i=1}^6 \left(\frac{(f_i - A \cdot fmod(z, E)_i)}{\sqrt{\sigma_i^2 + (0.1f_i)^2}} \right)^2 \quad (1)$$

The index i refers to the six fluxes, f_i is the measured flux and $fmod(z, E)$ is the flux predicted by a template at a redshift of z and extinction E(B-V) = E. Since this is not a formal χ^2 calculation the quantitative probabilities associated with χ^2 values are not strictly valid. The normalization constant A minimizes $\chi(z, E)^2$.

$$A = \sum_{i=1}^6 \frac{f_i \cdot fmod(z, E)_i}{\sigma_i^2 + (0.1f_i)^2} / \sum_{i=1}^6 \frac{(fmod(z, E)_i)^2}{\sigma_i^2 + (0.1f_i)^2} \quad (2)$$

The limit of the expression at very low flux levels is the standard form with the formal background, σ , dominating the denominator and at high flux levels it is the flux difference between the observations and the model divided by 10% of the flux instead of the σ . At high flux levels the errors in the fit are proportional to flux since the dominate errors are intra-pixel sensitivity variations and systematic flux errors. The accuracy of the NICMOS flux levels may be better than this. It is estimated to be 4 - 5% for this level of dithering but the output does not appear to strongly depend on the precise coefficient of the flux in the denominator of equation(1).

4.1. Photometric Redshift Accuracy

Photometric redshifts have gained a reasonable reputation for accuracy, particularly at high redshifts where the clear signature of the Lyman break is easy to observe. Two tests of the photometric redshifts derived in this work are comparison to available spectroscopic NHDF redshifts and comparison with previous NHDF photometric redshifts (TWS,

Fernández-Soto, Lanzetta, & Yahil (1999), Wang, Bachall, & Turner (1998)).

4.1.1. Comparison with Spectroscopic Redshifts

The primary source of spectroscopic redshifts is Cohen et al. (2000), enhanced and modified by Cohen (2001). The small reductions in the field area described in § 2 reduces the number of comparison redshifts to 135. Figure 3 shows the results of the comparison. The standard deviation is 0.29 in redshift, however, it is not constant with redshift. Most of the error occurs in the redshift range between 0 and 2, as is expected, since the prominent Lyman break does not appear in our data for that range. Note that galaxies in the redshift range between 0 and 0.5 are not used in this study.

Catastrophic redshift errors, errors of more than 0.5 in redshift, are overplotted with squares in Figure 3. Analysis of the 11 catastrophic failures reveals three basic types of failures. The first type is where there is no clear minimum in the χ^2 value along the range of redshifts, extinctions or SED templates. These are characterized by a steadily decreasing χ^2 value with a parameter, such as template, until the end of the parameter space is reached. This failure of the parameters to span the space of galaxy types is seen in 6 galaxies. The second category contains 5 galaxies that are most probably superpositions of two galaxies that have not been separated by the SE source extraction process. Both galaxies are contained in the LRIS 1" slit width used in the spectroscopic observations (Cohen et al. 2000). In this case the spectroscopic redshift would be determined by the galaxy with the most prominent spectral features while the photometric redshift would be most influenced by the galaxy with the highest continuum level.

The third failure in 2 galaxies is an apparent mild degeneracy in parameters which tends to favor a redshift of about 0.5 for galaxies with spectroscopic redshifts between 0.5 and 1.0. These galaxies appear to be well fit at the correct redshift with an intermediate SED and low value of extinction or at a redshift of ~ 0.5 with a very hot template and a high value of extinction. This degeneracy creates a pile up of galaxies at redshifts of 0.48 and 0.56. Examination of the photometric redshifts for these sources where the extinction is forced to be zero did not give statistically better fits except in the extreme cases such as those in Table 1. This type of error can reduce the calculated SFR in the redshift 0.5 to 1.5 bin by moving some sources out of the bin to a redshift of 0.48 or reducing the calculated UV flux for a source that has been moved to a lower redshift erroneously. This would make the SFR for redshift a lower limit, subject to other errors. Note that some galaxies have multiple failure modes so that the number of failures listed is larger than the number of failed galaxies.

Table 1 lists the 11 galaxies with redshift errors larger than 0.5 along with their parameters and the probable cause of the error. The general conclusion is that the photometric redshifts are quite adequate for statistical studies but can be subject to significant errors for individual galaxies.

4.1.2. Comparison with Previous Photometric Redshifts

The comparison between the spectroscopic and photometric redshifts is dominated by low redshift fairly bright galaxies except for the few faint, high redshift galaxies that have spectroscopic redshifts through very long spectroscopic observations on the largest ground based telescopes. It might be expected that the agreement on bright sources may be better than for the more numerous faint galaxies. One test is a comparison between the photometric redshifts obtained in the Deep NICMOS field (TWS) with those found in this study. The NICMOS F110W and F160W images are completely independent between the two data sets while the WFPC2 image are in common except that KFOCAS was used for source extraction in TWS and SE is used here. The comparison primarily determines the differences introduced by noise in the F110W and F160W images. Redshifts from the NICMOS deep NHDF images should be more accurate than the redshifts from the present study due to the higher signal to noise of the deep images.

A total of 283 galaxies in the Deep images also appear as legitimate galaxies in this set of images. Figure 4 shows a histogram of the differences in the redshifts between the deep and present images. The differences are peaked at zero as expected but do not appear to be a Gaussian distribution away from the peak. The differences are reasonably equally distributed between positive and negative values with a slight skew toward negative values (the present redshift higher than the deep redshift). The percentage of "catastrophic failures", a difference greater than 0.5, is 17%. Some of the failures create large differences in redshift. Examination of some cases with large differences reveals significant differences in either the F110W or F160W flux. As expected there is little variation in the WFPC2 fluxes measured by KFOCAS and SExtractor. The 17% significant redshift error from this comparison is higher than the 8% error found from the spectroscopic redshift comparison. In the final error analysis we will assume that 17% of the galaxies have redshift errors that are randomly distributed up to a maximum of 4.

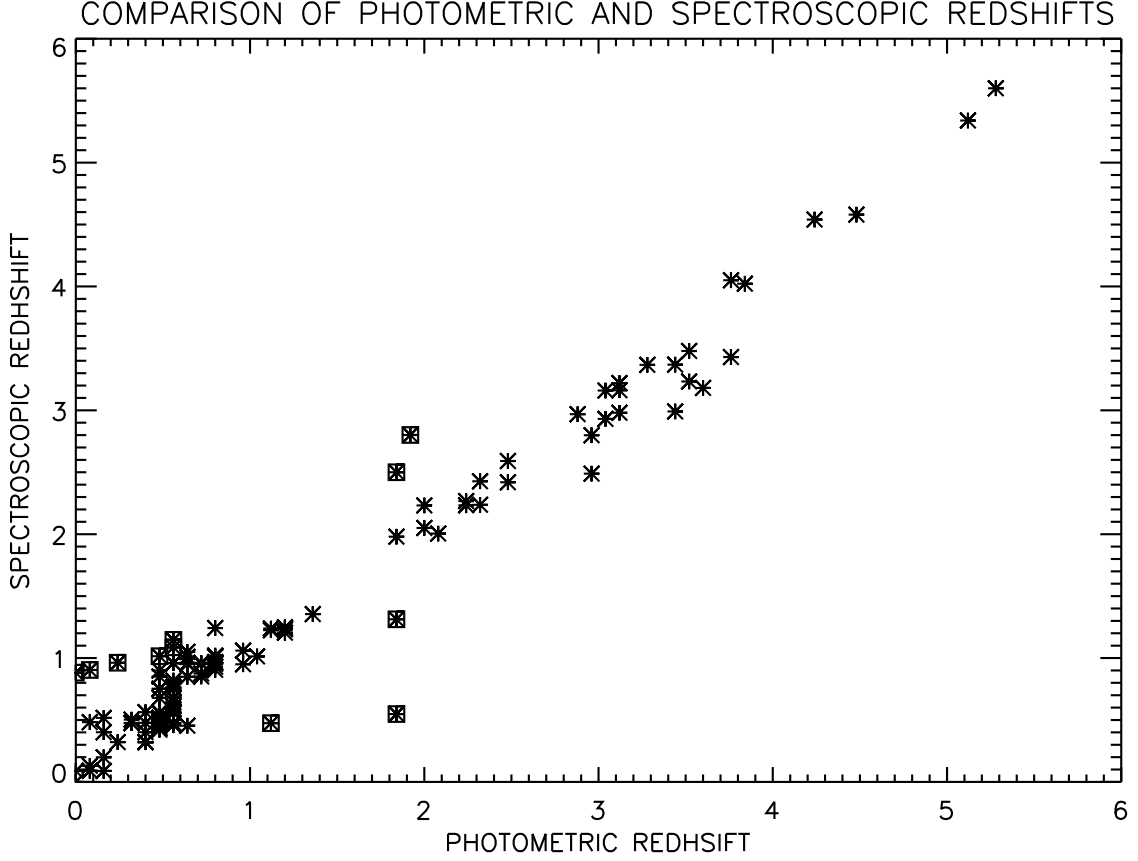


Fig. 3.— Plot of the spectroscopic redshifts from Cohen et al. (2000) versus the photometric redshifts determined in this work. Some high redshift objects have been added from other sources. Objects that have redshift differences greater than 0.5 are overplotted with a square symbol and are discussed in the text and Table 1.

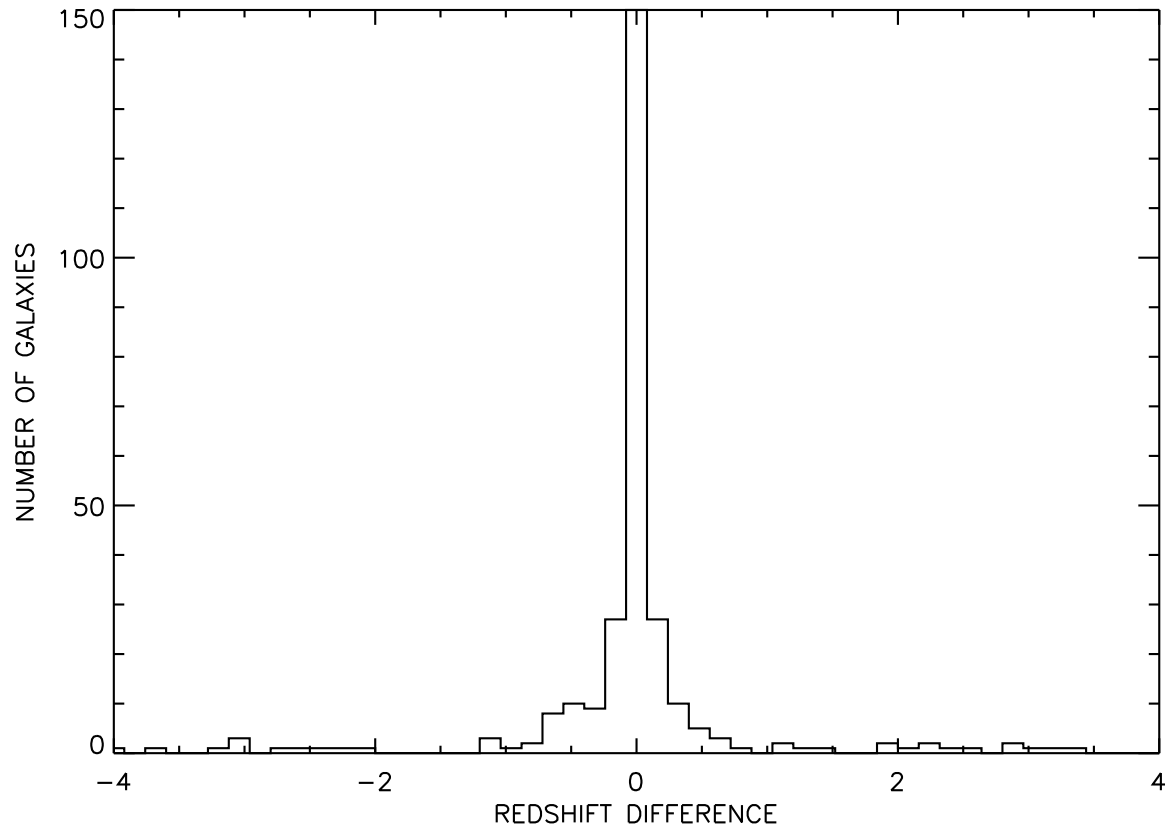


Fig. 4.— A histogram of the values of the Deep NICMOS NHDF photometric redshifts minus the photometric redshifts determined from this study.

4.1.3. Comparison with Photometric Redshifts from Other Work

There have been several other determinations of photometric redshift in the NHDF but only two (Wang, Bachall, & Turner 1998; Fernández-Soto, Lanzetta, & Yahil 1999) have readily accessible catalogs of redshift and object position. Figure 5 shows the comparison between this work and the redshifts obtained by the two groups. Coincidence of objects was determined by position correspondence within $0.3''$. The redshifts of both previous studies are offset to larger redshifts than this study. This effect is most probably due to both groups not correcting for extinction. Without extinction the only mechanism to make a galaxy redder is to redshift it or choose an earlier template.

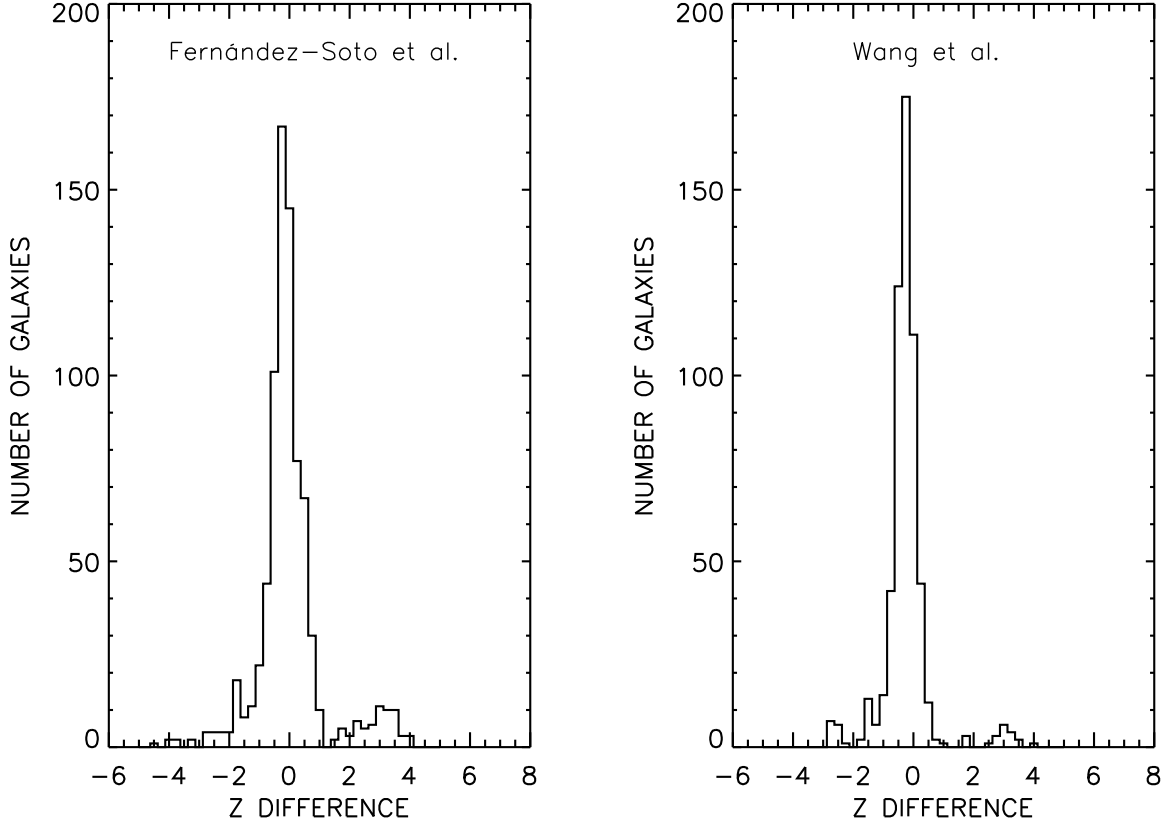


Fig. 5.— Histograms of the values of the photometric redshifts determined from this study minus the redshifts from Fernández-Soto, Lanzetta, & Yahil (1999) on the left and Wang, Bachall, & Turner (1998) on the right. In both case the redshifts from the cited works were subtracted from the redshifts found in this work.

5. Catalog of Individual Source Properties

Table 2 lists the individual sources, ordered by RA, that satisfy the criteria listed in §5.1. Column 1 gives the NICMOS identification number. Column 2 is the WFPC2 identification number of the galaxy from Williams et al. (1996) if there is positional coincidence within $0.3''$. Columns 3 and 4 are the redshift and extinction. Column 5 contains the SFR in solar masses per year as determined in § 6. The bolometric luminosity of the galaxy is in column 6. The flux of a galaxy is obtained by integrating over the unextincted selected template scaled by the factor A from equation (2). The bolometric luminosity then follows from the redshift and our adopted cosmology. The fraction of the luminosity that is extincted and therefore goes into far infrared flux is in column 7 followed by the calculated 6, 15 and $850\ \mu\text{m}$ flux (mJy) in columns 8, 9 and 10 for comparison with measured ISO and SCUBA fluxes (§ 10). The luminosities, ISO fluxes and SCUBA fluxes of galaxies with a redshift of zero are all set to zero.

Columns 11 and 12 give the template number T of the best fit, and the modified χ^2 value of the fit from Equation 1. It should be noted that the distribution of the modified χ^2 values will not rigorously follow a true χ^2 distribution. The values are provided to give a qualitative indication of the relative goodness of fit for the best fit values of redshift, template type and E(B-V). Column 13 has the total F160W AB magnitude, determined by adding all of the pixels designated by SE as part of an object, followed by the 0.6 aperture F160W magnitude (Ap. mag) in column 14. Note that variations in local background as interpreted by SE can result in an aperture magnitude brighter than a total magnitude for faint galaxies. If no F160W magnitude is listed the object had a zero or negative measured F160W flux. Columns 15 and 16 are the right ascension and declination positions of the object. The RA listing contains only seconds and the DEC listing only minutes and seconds. $12^{\text{h}}\ 36^{\text{m}}$ should be added to the RA and 62° to the DEC. Note that a few sources have RA values of $12^{\text{h}}\ 37^{\text{m}}$ plus seconds. These sources are found at the end of the catalog with seconds values between 0 and 1.2.

5.1. Source Selection Criteria

Data reduction is performed on all sources detected by the Szalay procedure. Additional criteria for source selection are introduced before sources appear in the catalog of objects used for determining the star formation history. First all sources that are known stars are rejected. Next all objects that are too near the edge of the image to insure that no flux is lost are rejected. This step uses the SE internal flags and visual inspection of the image. Next a list of suspect objects are rejected from a visual inspection of the images. These

include objects with significant overlap that have been counted as a single object by SE and stellar diffraction spikes that were counted as objects. Next all objects with SE internal flags of 16 or greater, indicating that the photometric aperture was corrupted by some means, are rejected. Next is a criterion that all valid sources must have a signal to noise of 3.5 or greater in one band or a signal to noise of 2.5 or greater in two bands. Finally an accepted source is required to have a flux greater than 5×10^{-4} ADUs per second in both the F110W and F160W bands. All sources that meet these criteria are included in the catalog but only sources with redshifts between 0.5 and 6.5 are used in the star formation history analysis.

Two other comments are in order on source selection. At this point, for the small number of objects that have known redshifts, the photometric redshift is replaced by the spectroscopic redshift in the analysis procedures. Second the bright galaxy NHDF 3-610 is rejected from the analysis due to impingement of the diffraction spike from the adjacent star and a clear overlap with another galaxy. For this reason, even though it is quite bright, it does not appear in Table 2.

5.2. Distribution of Source Properties

Figure 6 shows the distribution of F160W magnitudes with redshift and the calculated tracks of an early, a late, and an extincted late L^* galaxy. The early galaxy is template 1.0, the late galaxy template 6.0 and the extincted late galaxy is template 6.0 with an extinction of $E(B-V) = 0.2$. The sources are color coded with the earliest type galaxy deep red and the latest galaxy deep blue as indicated by the legend on the figure. As expected the majority of the early type galaxies lie at low redshift with some intermediate type galaxies up to redshifts of five. The majority of galaxies have template numbers between 5 and 6.

Particularly at low values, there is apparent redshift banding. The band at zero redshift is due to galaxies with χ^2 values that were still falling as they approached zero redshift, indicating that they were not matched by any of the galaxy templates. The band at redshift 0.5 does correspond to an over density observed in the spectroscopic redshift analysis of Cohen (2001) which also sees a small over density at a redshift of 1. It is tempting to interpret the banding in Figure 6 as sheets or nodes in large scale structure encountered by the pencil beam of the NHDF but the redshift analysis in § 4 does not seem to warrant that interpretation. This is particularly true for the band at 0.5 which may be due to the effect discussed in § 4.1.1. Investigation of the significance of the banding will be deferred to a later paper.

Most of the galaxies in Figure 6 fall above the lines of the L^* ($3.4 \times 10^{10} L_{\odot}$) galaxy

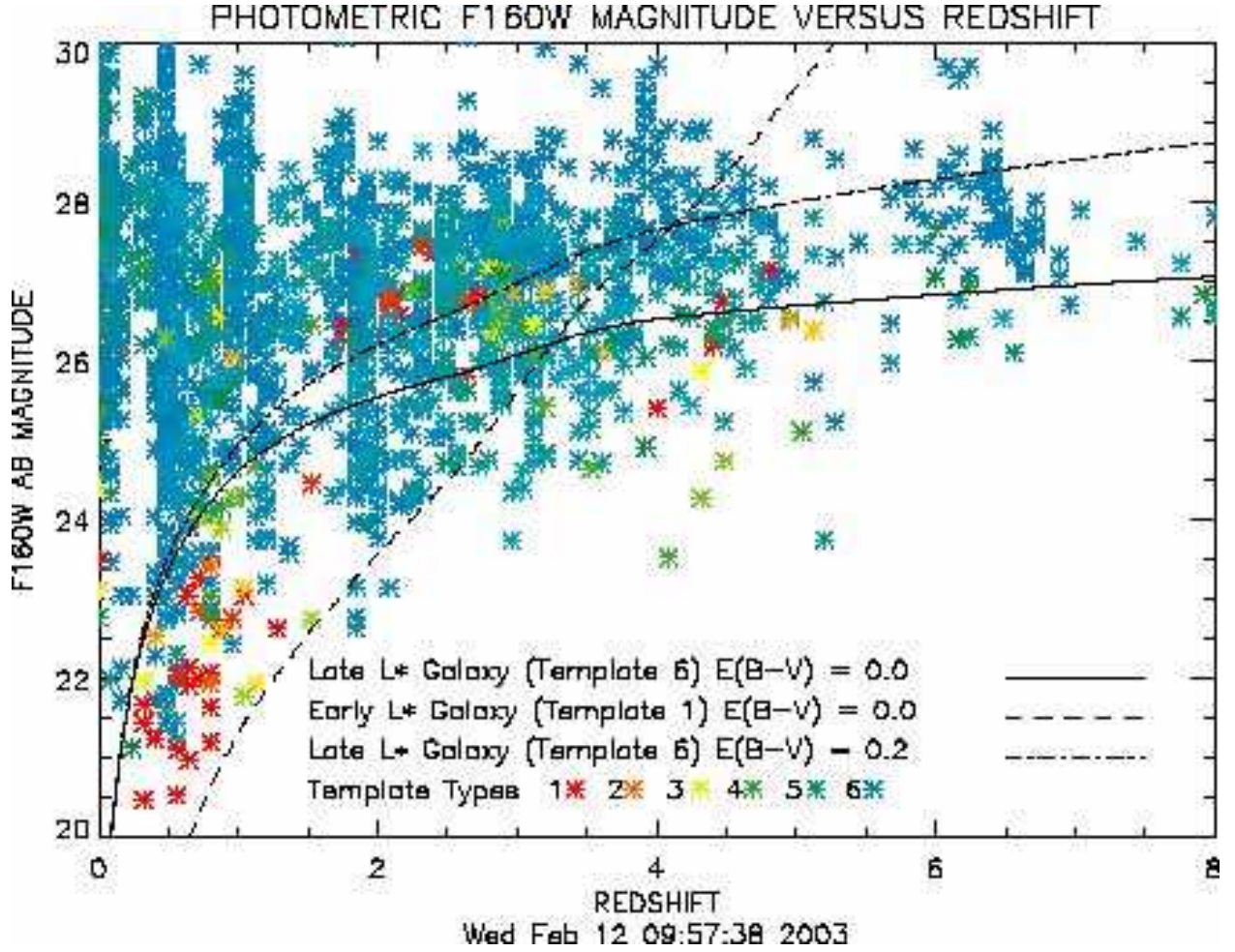


Fig. 6.— The distribution of F160W AB 0.6'' diameter aperture magnitudes versus photometric redshift. The solid and dashed lines indicate the F160W aperture magnitude of an early and late-type L* galaxy. The dash dot line shows the track of a late-type L* galaxy with an extinction of $E(B-V)$ equal to 0.2. L* is defined as a total luminosity of $3.4 \times 10^{10} L_{\odot}$

tracks. Past a redshift of ~ 3 there are several galaxies that lie significantly below the L^* galaxy line. This is expected since there certainly are galaxies brighter than L^* . It is legitimate to ask whether these galaxies have non-physical parameters and whether their position in the diagram is due to a bad fit with the models. Fig. 7 shows the fit between the observed fluxes of the 9 galaxies that most exceed L^* and the best fit fluxes from the photometric redshift program. In all cases the fit is excellent, therefore, their position in the diagram is not due to a bad fit. Table 3 gives a summary of the properties of the nine sources. Although all but one galaxy has the luminosity of a Luminous InfraRed Galaxy (LIRG), the low extinction does not re-emit a large enough fraction of the luminosity to put them in that category. All but 2 galaxies fall in the top 50 most luminous galaxies in the field but none of them are in the top 10. This leads to the conclusion that the physical properties of the galaxies are realistic and that there is no reason to exclude them as legitimate sources based on non-physical parameters.

Note that 398.0 and 410.0 are probably two parts of the same galaxy. Their photometric redshifts of 3.04 and 2.96 are similar but not exactly the same. The spectroscopic redshift for the galaxy is 2.799, close to the photometric redshift. The spectroscopic redshift is the redshift used in calculating the luminosity for source 410. If the spectroscopic redshift for source 410 is also the proper redshift for source 398, the 398 luminosity should be reduced by a factor of 0.74.

There are three sources without equivalent WFPC2 identifications. Source 398 is an extension of source 410 identified as WFPC2 4-555.1. The closest WFPC2 source to 398 is actually 4-555.11 which is $0.32''$ away, just beyond our association radius of $0.3''$. Similarly the closest WFPC sources for 1630 and 1636 are 3-367.0 ($0.33''$) and 3-839 ($0.40''$). Although not listed in Table 2, the identifications are listed in Table 3 since inspection of the images clearly indicates that they are the proper associations. It is often the case that the F160W center of a galaxy is offset from the optical position. The F160W position is more representative of the underlying stellar distribution while the optical position measures rest frame UV star formation activity.

6. Determination of the Star Formation Rates

As in TWS the SFR is determined from the broad band 1500 \AA flux relation given by Madau, Pozzetti & Dickinson (1998).

$$UV_{1500} = 8.0 \times 10^{27} \cdot SFR(M_{\odot}/yr) \text{ ergs second}^{-1} \text{ Hz}^{-1} \quad (3)$$

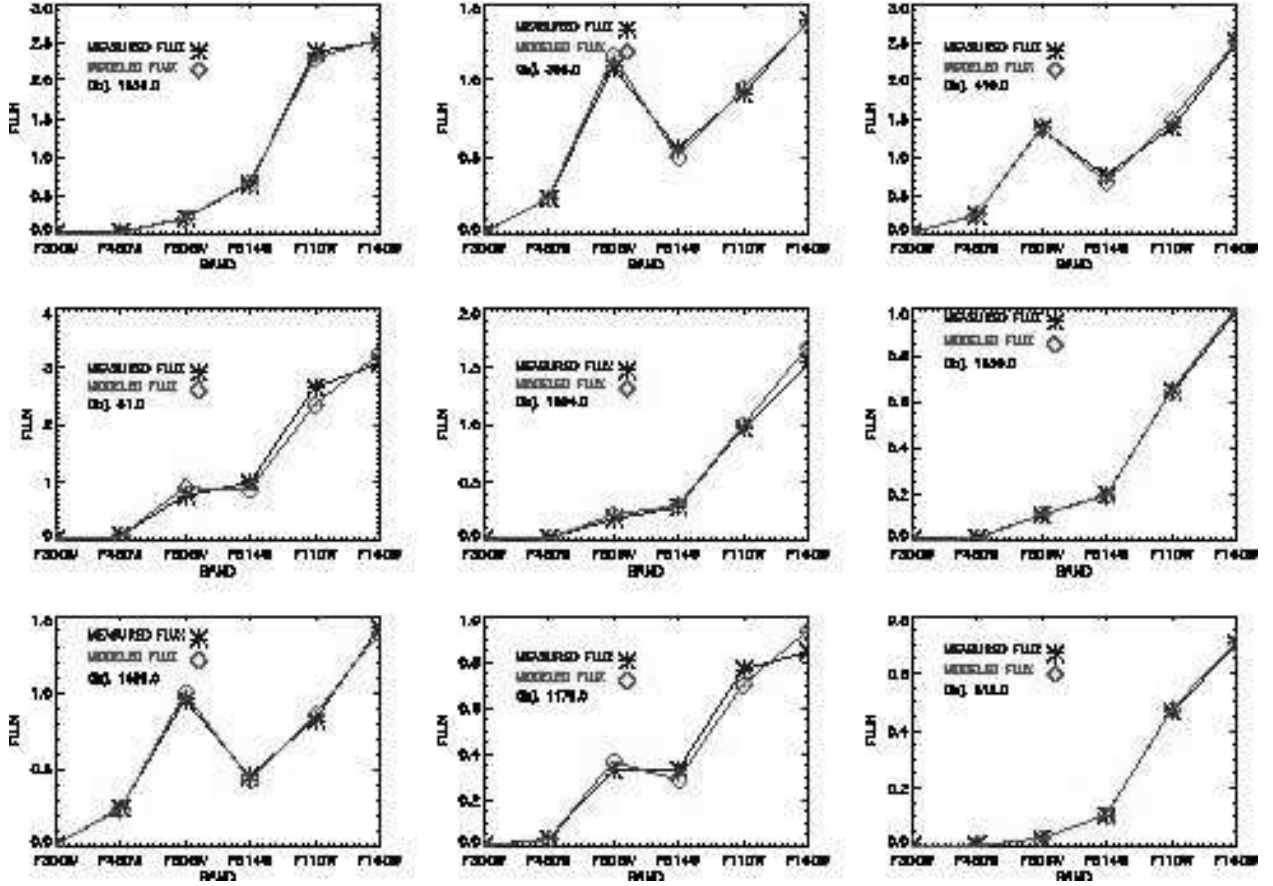


Fig. 7.— The best fit fluxes matched to the observed fluxes for 9 galaxies that are significantly brighter than the L^* galaxy line. Luminosities are given in L_\odot .

The value of the UV flux is determined from the 1500 Å flux of the *unextincted* template found in the χ^2 analysis averaged over a 200 Å band centered on 1500 Å. The reshift and the normalization factor A (equation 2) set the absolute 1500 Å flux. This procedure provides the extinction corrected 1500 Å flux for the SFR calculation. It is obviously a simplification to assume a single extinction for a whole galaxy but it is clearly better than assuming a single average extinction for all galaxies or no extinction at all. A much more extensive discussion of the extinction is presented in TWS and it is not repeated here.

Rather than using the isophotal or total flux values returned by SE, the flux in each band is computed as the sum of the flux from each pixel that the Szalay procedure and SE determine is part of an object. The SFR computed with the A value determined from the 0.6'' aperture is then multiplied by the ratio of the total flux to the aperture flux to give the values reported in Table 2. The sum of the SFRs in Table 2 gives the observed SFR in the appropriate redshift bins. At high redshift the observed SFR is significantly below the actual SFR due to surface brightness dimming. The correction for this effect, using the extinction corrected star formation rate per pixel is described in § 7.

7. Correction for Surface Brightness Dimming

It is well known that surface brightness dimming at high redshifts limits the number as well as the extent of galaxies that are detected, creating errors in the measured SFR. In TWS we used the star formation intensity distribution function (Lanzetta et al. 1999) to correct for star formation missed due to surface brightness dimming. Lanzetta et al. (2002) has also used the distribution to correct for missed star formation but did not use a distribution derived from extinction corrected UV fluxes.

7.1. Star Formation Intensity Distribution Function

The star formation intensity x is defined as the SFR in solar masses per year per *proper* square kiloparsec. The intensity is calculated for each pixel that is part of a galaxy. Within a given redshift interval the distribution function, $h(x)$, is defined as the sum of all the proper areas in a interval of specific intensity, divided by the interval and by the comoving volume in cubic megaparsecs defined by the field and redshift interval (Lanzetta et al. 1999). Defined in this manner the values of $h(x)$ determine the star formation rate per cubic comoving megaparsec through equation(4).

$$sfr = \int_0^\infty xh(x)dx \quad (4)$$

The distribution functions for both extinction corrected and uncorrected star formation intensities are shown in Figure 8.

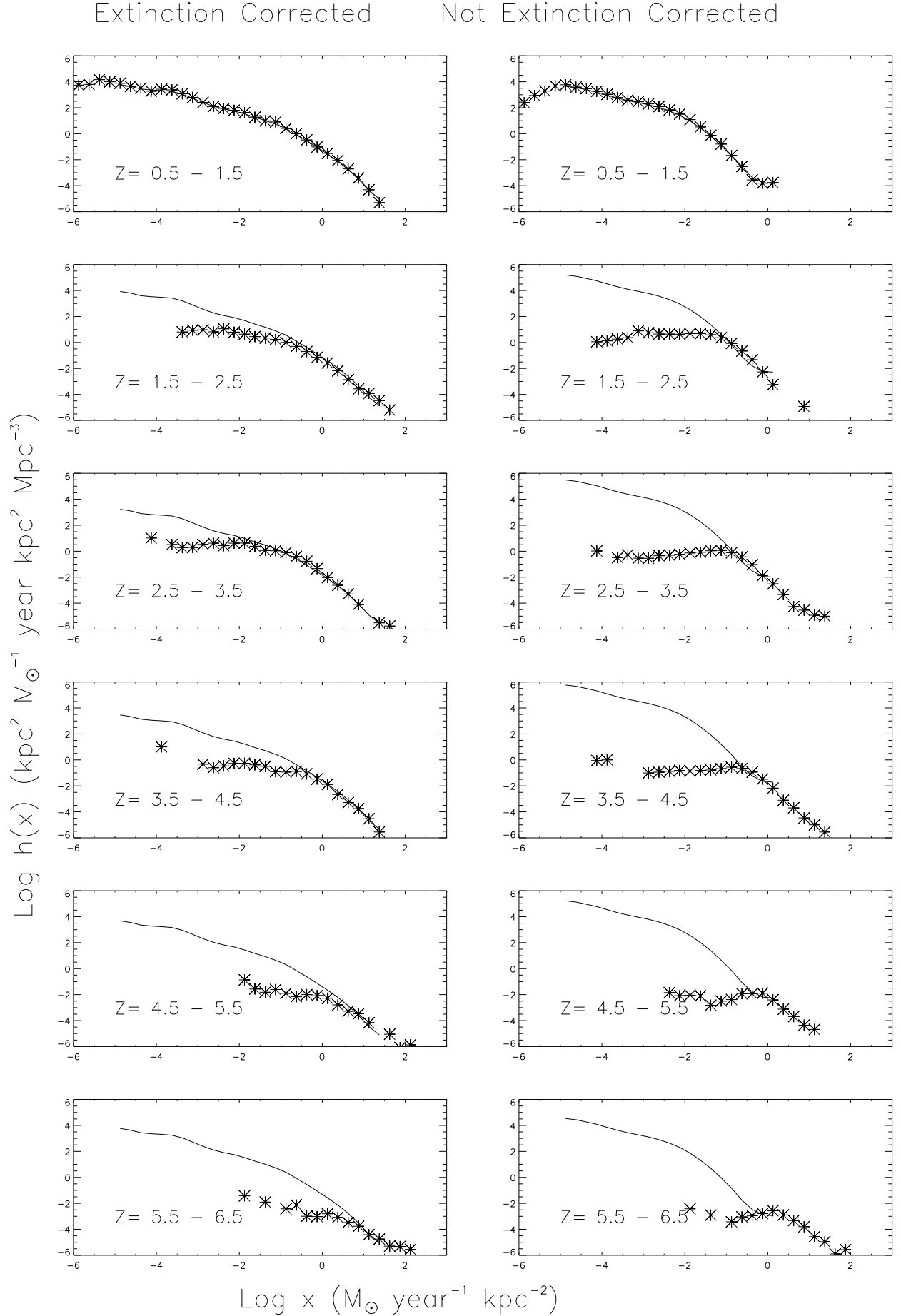


Fig. 8.— Plots of the SFR intensity distribution for the Northern HDF. The abscissa is

The top panels of Figure 8 show the 3 point smoothed fit to both the extinction corrected and uncorrected distribution function at a redshift of 1. At higher redshifts the smoothed curve is matched to the high intensity portion of the distribution by simply moving the smoothed distribution up or down in the log-log plot. It is clear that the smoothed curve for the uncorrected distribution does not match well at higher redshifts. This is discussed further in § 7.3 but for now we will concentrate only on the extinction corrected distribution.

The deviation of the observed data from the smoothed distribution in the lower panels shows the effect of surface brightness dimming. As in TWS we correct for surface brightness dimming by integrating equation(4) over the observed data where the smoothed function matches the data and then over the smoothed function (adjusted in height) when the observations fall below the curve. Note that the integral reaches 59% of its total value at $\log x = -0.25$ and 94% of its total value at $\log x = -1.25$. § 7.3 discusses the validity of the correction.

Table 4 shows the SFR at each stage of correction. The second column gives the rate with no correction for either extinction or surface brightness dimming. The third column shows the SFR after correction for extinction only and the fourth column shows the SFR after correction for both extinction and surface brightness dimming. At low redshifts extinction is the dominant correction while at high redshifts extinction and surface brightness dimming are comparable. All of the calculations without extinction correction are made from the output of the χ^2 photometric redshift program with the extinction held to zero. In some cases this alters the photometric redshift since the degree of freedom to redden a galaxy by extinction is removed. This is the cause of the odd case at redshift 4 where the extinction corrected SFR is less than the uncorrected SFR.

7.2. Selection Function

Lanzetta et al. (2002) introduced the concept of a selection function in conjunction with the star formation intensity distribution function $h(x)$. The selection function is the angular area over which a parameter at a given depth can be detected. The maximum angular area is the total area of the observation. At some depth of a parameter such as flux, the area goes to zero when it becomes undetectable. The parameter used in (Lanzetta et al. 2002) and here is the star formation intensity x . The main reason for introducing this concept is the variance in sensitivity of the NICMOS Camera 3 in different regions of the detector. The sensitivity varies by a factor of 3 from maximum to minimum.

The star formation intensity is a function of redshift, SED, extinction, and flux, there-

fore, each pixel included in $h(x)$ at a specific x may have a different selection function depending on the values of the parameters. Given the criterion of 3.5 sigma detection in a flux band for 3 contiguous pixels the selection function determines for each source pixel the percentage of the field area where the source could be detected. The star formation intensity distribution function program then corrects the area of each pixel by the inverse of the selection function. The maximum allowed correction is a factor of 10 to prevent marginal detections from dominating the distribution function. In practice only a small percentage of pixels have selection functions less than 100%.

7.3. Validity of the Distribution and Comparison With Other Work

Initially in TWS the star formation intensity distribution was treated strictly empirically with no physical motivation. The identical match of the smoothed distribution derived here from largely independent data is further empirical confirmation of the distribution as is the excellent match at high SFR intensities at higher redshifts. Thompson (2002), however, provides a physical motivation by showing that the distribution is a natural consequence of the Schmidt law, the majority of star formation occurring in exponential disks, and a Schechter distribution of galaxy masses. It also showed that effects of a smaller characteristic mass and a smaller average radius of the exponential disk at higher redshift have opposite effects on the shape of the distribution leading to a generally invariant distribution. Although we lack detailed knowledge of the changes of characteristic mass and exponential disk radius with redshift, the assumption of an invariant distribution appears to be justified. Even if the surface brightness dimming corrections in Table 4 varied by 30% the error would be small compared to the errors from other effects such as photometric error and large scale structure.

Lanzetta et al. (2002) also utilized the star formation intensity distribution function to correct for surface brightness dimming but found a SFR that steadily increases from the present day to high values at a redshift of 8, in contrast to the essentially steady star formation rate between a redshift of 1 and 6 as presented in § 8. Only the SFR in the common ground of redshifts will be discussed in the following comments. The comparison will be with the rates found from scaling the $h(x)$ distribution vertically in Lanzetta et al. (2002) since that is the technique used in this paper.

The critical difference between the technique applied here versus Lanzetta et al. (2002) is that this work uses the extinction corrected distribution where as Lanzetta et al. (2002) use the distribution that is uncorrected for extinction. Lanzetta et al. (2002) refer to this rate as the unobscured rate. At a redshift of 1 they find a SFR of $0.03M_{\odot}$ per Mpc^{-3} whereas the value in this work is $0.3M_{\odot}$ per Mpc^{-3} . This is simply understood as the

difference between correcting for extinction and not correcting for extinction. At a redshift of 4 Lanzetta et al. (2002) find a rate of $0.25 M_{\odot}$ per Mpc^{-3} comparable to our value of 0.1. At a redshift of 6 they find a value of 0.45 compared to our value of 0.2.

The difference between our relatively steady values and their increasing values is due to two effects. As can be seen from Figure 8 and Lanzetta et al. (2002) the bright end of the distribution has a steeper slope in the uncorrected for extinction case than the corrected one. This is due to extinction removing intrinsically bright pixels from the distribution. Second at higher redshifts the average extinction of the sample becomes smaller due to surface brightness dimming removing the highly extincted galaxies from the sample. Matching the steep slope of the uncorrected distribution function to the continuously lower extinction sample at higher redshifts results in an over correction and an apparent steadily increasing star formation rate. Figure 8 shows this effect. The dimming correction in the right hand column is significantly higher than in the left hand extinction corrected column.

8. Star Formation History

Initial work on the star formation history of the universe by (Madau et al. 1996) showed a sharp rise in SFR from the present day to a peak at z between 1 and 2 then a decline to lower rates at higher redshifts. Later work by Madau, Pozzetti & Dickinson (1998), which applied a small correction for extinction, showed a shallower decline in SFR at high redshifts. Subsequent work by Steidel et al. (1999), Hopkins, Connolly, & Szalay (2000) and TWS gave SFRs that were roughly constant at redshifts higher than 1. This is consistent with the results presented here. The SFR values found in this paper are also consistent with the SFRs found in the sub-millimeter observations of Barger et al. (2000) at redshifts of 1-3 and 3-6. The concordance of results between the various studies is discussed in § 11.

Figure 9 shows the SFR versus redshift corrected for the surface brightness dimming and the selection function as described in § 7. The redshift binning unit is 1 centered on integer redshifts. The lowest redshift included in the study is 0.5 and the highest is 6.5. The NHDF statistics are not adequate at redshifts below 0.5 to determine an accurate SFR. In that redshift range the number of sources is low and the percentage error in redshift is high, leading to high SFR errors. The accuracy of large area ground based surveys is much greater in this redshift range. Although Figure 6 shows galaxies at redshifts above 6.5 we do not use them in this analysis.

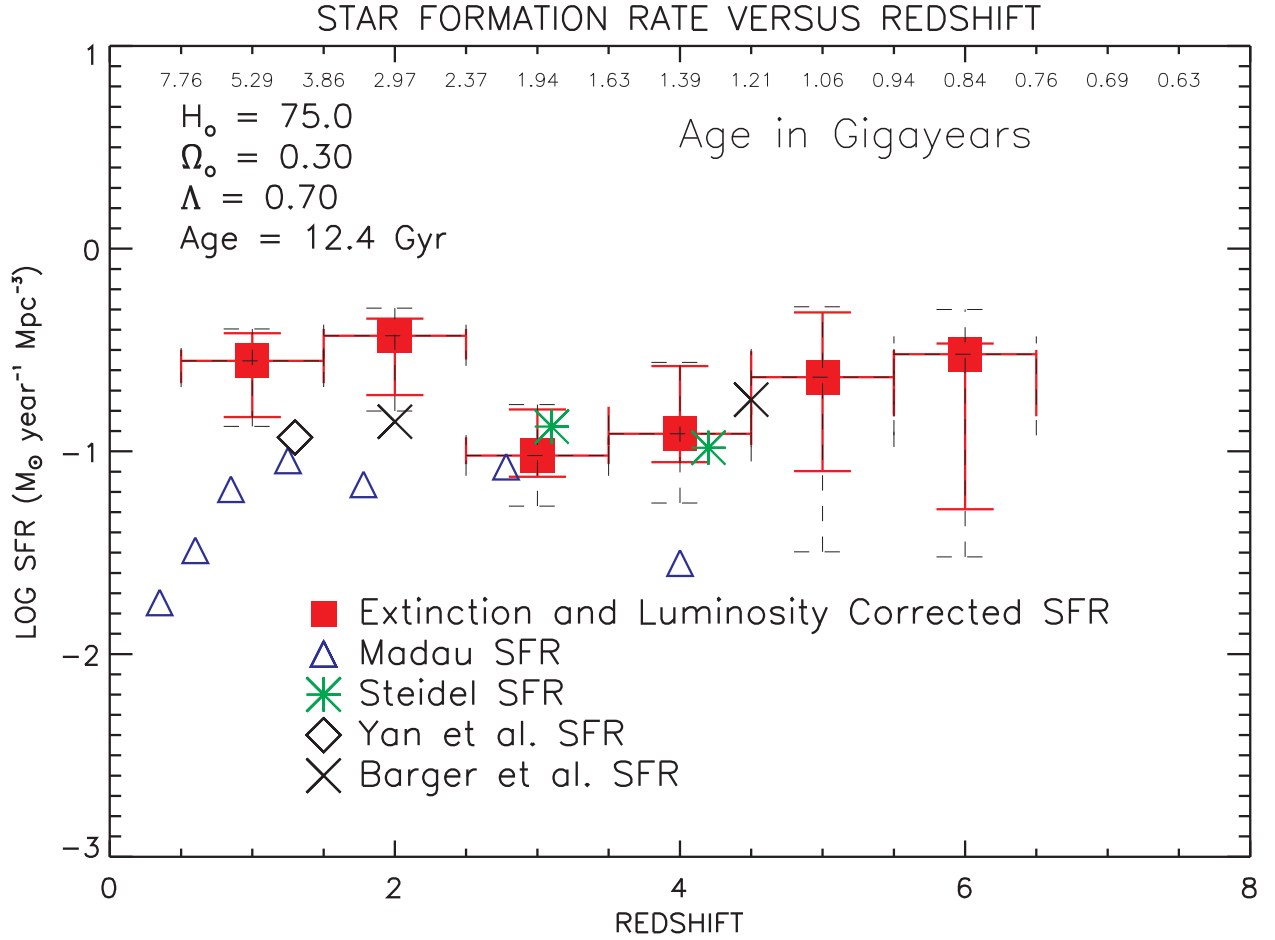


Fig. 9.— Plots of the extinction and surface brightness dimming corrected SFR as a function of redshift. The solid error bars indicate the photometric errors and the dashed error bars indicate the uncertainty in the global SFR. The SFR from Yan et al. (1999) indicated by the diamond is for star formation in the range between a redshift of 0.8 to 2.0. The SFRs from Barger et al. (2000) are indicated by the crosses and are for redshifts 1-3 and 3-6 with a $\Lambda = 2/3$ universe.

8.1. Star Formation Time History

The usual form of the ‘Madau Diagram’ plots SFR versus redshift since redshift is the measured quantity and is not subject to the choice of cosmology. This form of the diagram can be misleading in terms of when the majority of star formation occurs since there is very little time at high redshifts. A more instructive plot is the star formation rate versus age of the universe. In the era of ‘precision cosmology’ one can dare to produce such a plot with reasonable assumptions on the cosmology. For ages in the redshift range of 0.5 to 6.5 Figure 10 indicates the measured SFR at ages of the universe between 1.25 and 7.25 gigayears. The non integer age units are dictated by the ends of the redshift range.

Within the errors the SFR is roughly constant from an age of the universe between 1 and 7 gigayears at a rate significantly above the present day rate. The trend of the data indicates an increase in the formation rate from 1 gigayear to 7 gigayears but the errors are too large to validate this impression. Note that the binning of the objects is quite different between the SFR versus redshift and versus age of the universe plots.

8.2. Error Analysis

The error analysis for this data set was carried out in the same manner as the analysis performed in TWS where there is an extensive discussion of the analysis procedures. Table 5 gives the error sources from number statistics, photometric error and large scale structure. The greatly increased number of sources in this data set has reduced number statistics to a negligible error compared to other error sources.

8.2.1. Photometric Error Propagation

Photometric errors can propagate into errors in redshift, extinction, and SED. These in turn create errors in the SFR. As in TWS, the photometric error analysis computes the SFR in each redshift bin for 100 runs of the data with the flux values of each object altered randomly by the gaussian distribution of the flux errors calculated for each object. The flux error is the total flux error which includes both the random and systematic error shown in the denominator of equation 1. Due to the variation of sensitivity across the NICMOS detector, the errors in NICMOS flux are calculated individually for each galaxy. The distribution of SFRs between the runs determines the SFR error level from photometric errors. The solid line photometric error bars in Figure 9 are the 16% and 84% points of the SFR distribution in quadrature with the 17% redshift error discussed in § 4.1. This procedure integrates the

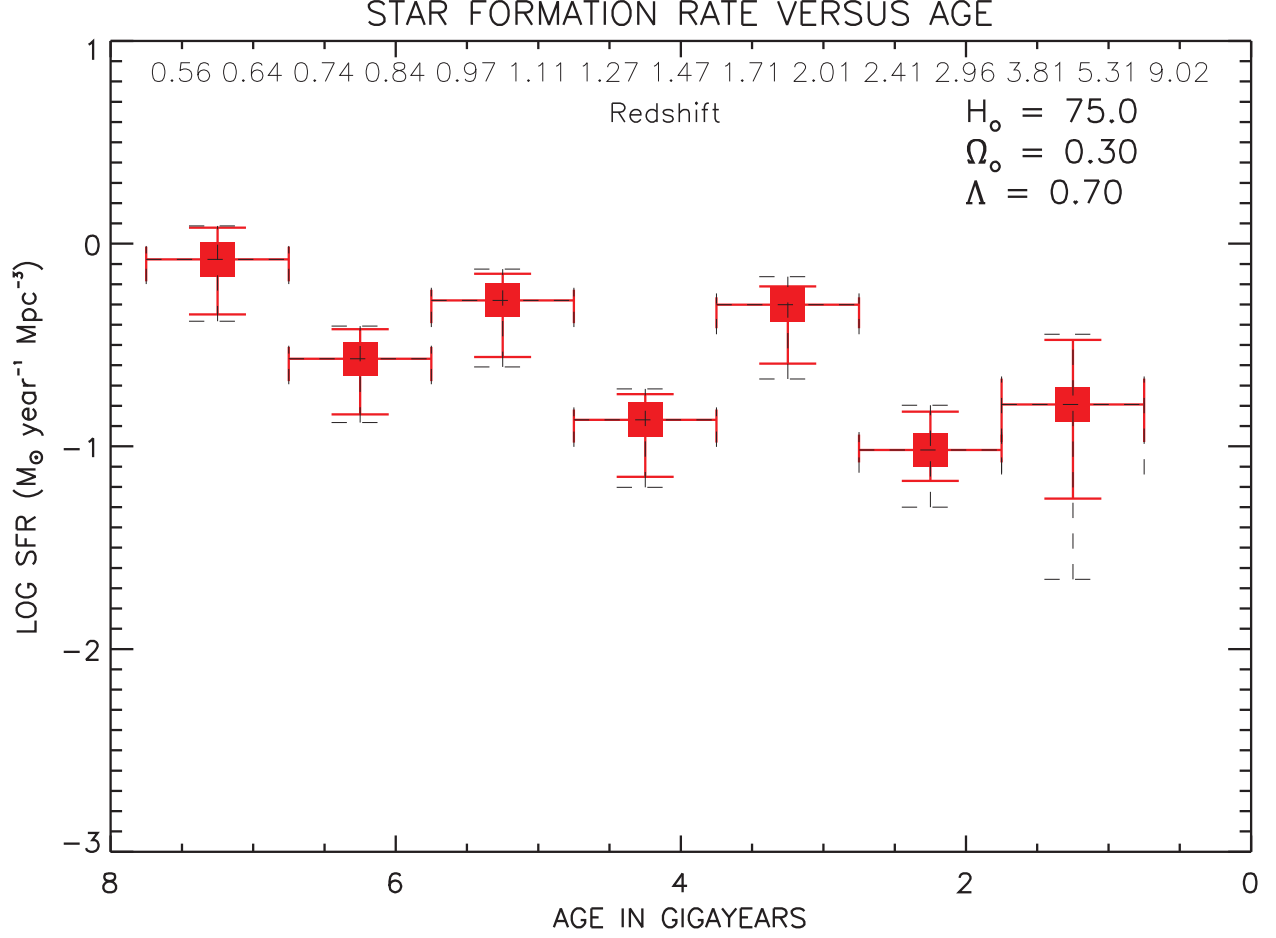


Fig. 10.— Plots of the extinction and surface brightness dimming corrected SFR as a function of age of the universe for the cosmology indicated in the figure. The solid error bars indicate the photometric errors and the dashed error bars indicate the uncertainty in the global SFR.

photometric error induced redshift, extinction and SED errors into a measured SFR error.

The procedure preserves the redshift, extinction, and SED calculated in each run, therefore, we can plot the individual errors in each parameter as a function of the F160W AB magnitude. Figures 11, 12 and 13 show the histograms of redshift, extinction and template SED errors in F160W AB magnitude bins ranging from 20 to 29 for all of the sources listed in Table 2. In each case the unperturbed value is subtracted from the perturbed value. Note that since the histograms include the more error prone objects in the 0.0-0.5 and 6.6-8.0 redshift ranges they are a conservative measure of the error.

The error histograms do not show any significant trend with magnitude. The basic reason is that the systematic part of the error scales with flux so that the perturbations for the strong fluxes are larger than for the weaker fluxes, accurately reflecting the observations. As mentioned in § 4, the 10% systematic error is probably an overestimation so errors at brighter magnitudes may be overestimations. If this is the case the error bars in Figure 9 may be exaggerated.

Both the redshift and extinction errors show a trend of being asymmetric around zero error with an over abundance of negative errors showing larger redshifts and extinctions for the unperturbed values than for the perturbed values. Both of these effects indicate larger SFRs for the unperturbed versus the perturbed values. This trend is reflected in the overall SFR errors shown in Figure 9 where the error bars extend further on the low side than the high side for most of the redshift bins.

8.2.2. Large Scale Structure Error

As in TWS the two-point correlation function $\xi(r_o, \gamma) = (r_o/r)^\gamma$ as given by Peebles (1980) is used to calculate the large scale structure error. The fractional error is taken as σ_N/N where

$$\sigma_N/N = \sqrt{1 + N \times I_2}/\sqrt{N} \quad (5)$$

and

$$I_2 = \int \int \xi(r_o, \gamma) dV_1 dV_2 / V^2 \quad (6)$$

For each redshift bin it is a very good approximation to consider the volume as a long thin tube of square cross section with sides of (comoving) dimension D and (comoving) length

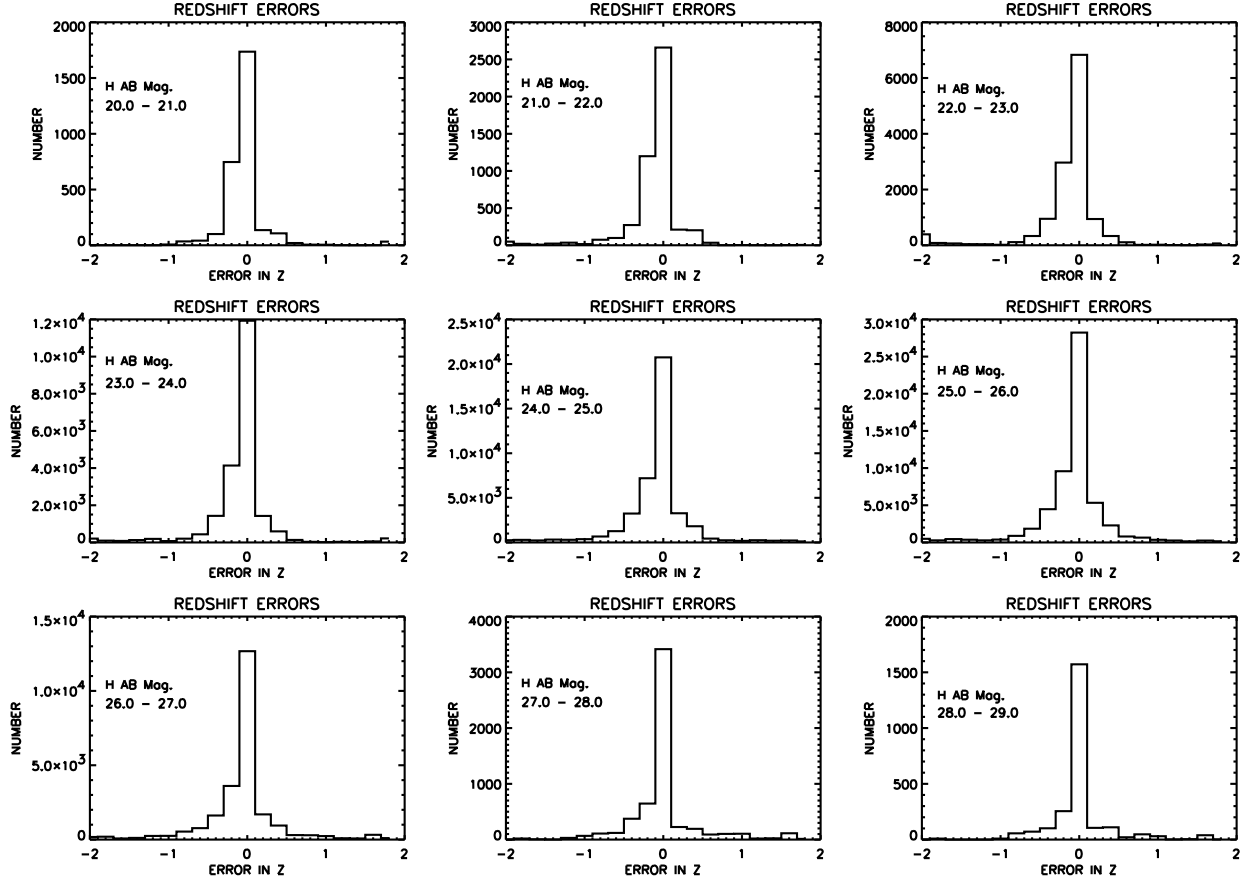


Fig. 11.— The redshift error histograms for all sources in Table 2. Negative values indicate that the unperturbed redshift is higher than the perturbed redshift.

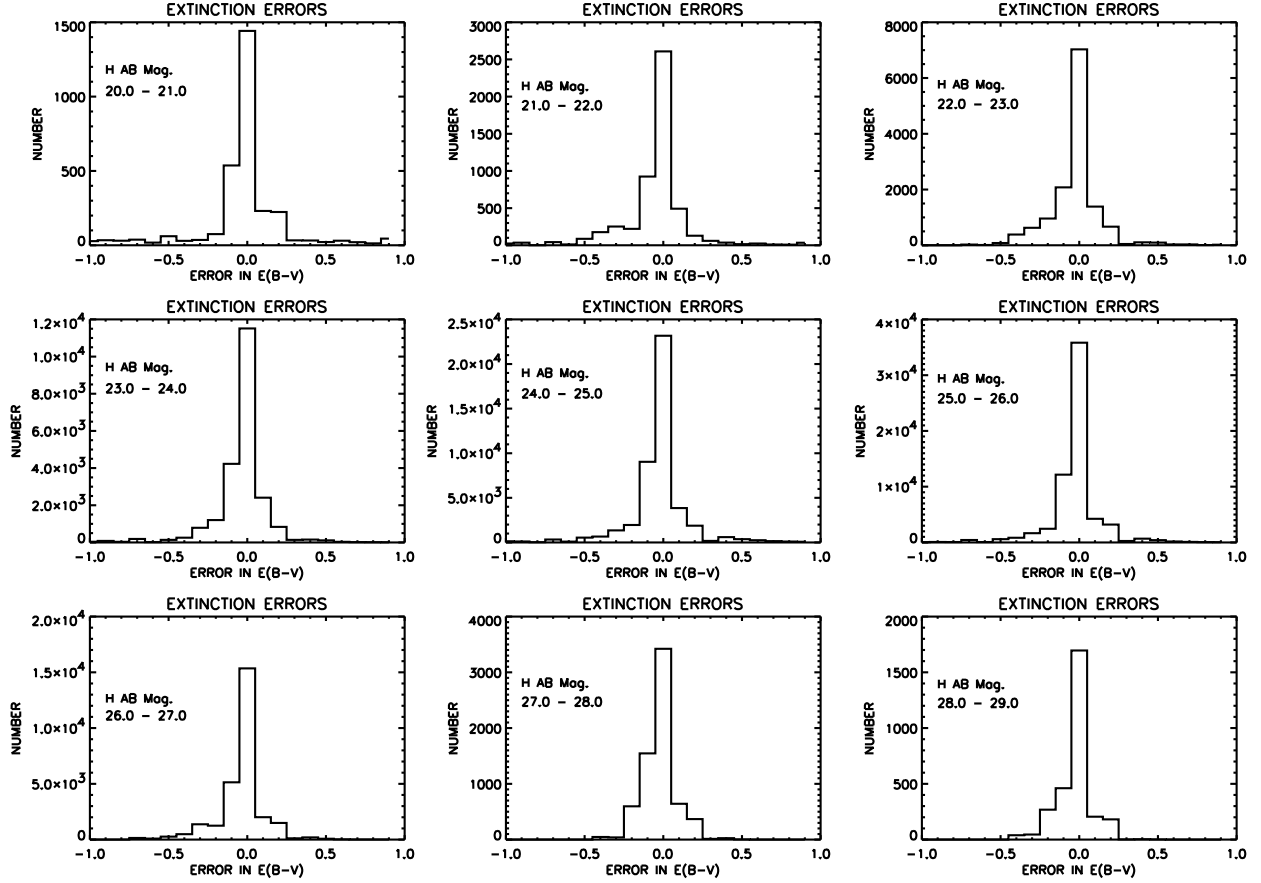


Fig. 12.— The $E(B-V)$ error histograms for all sources in Table 2. Negative values indicate that the unperturbed extinction is higher than the perturbed extinction.

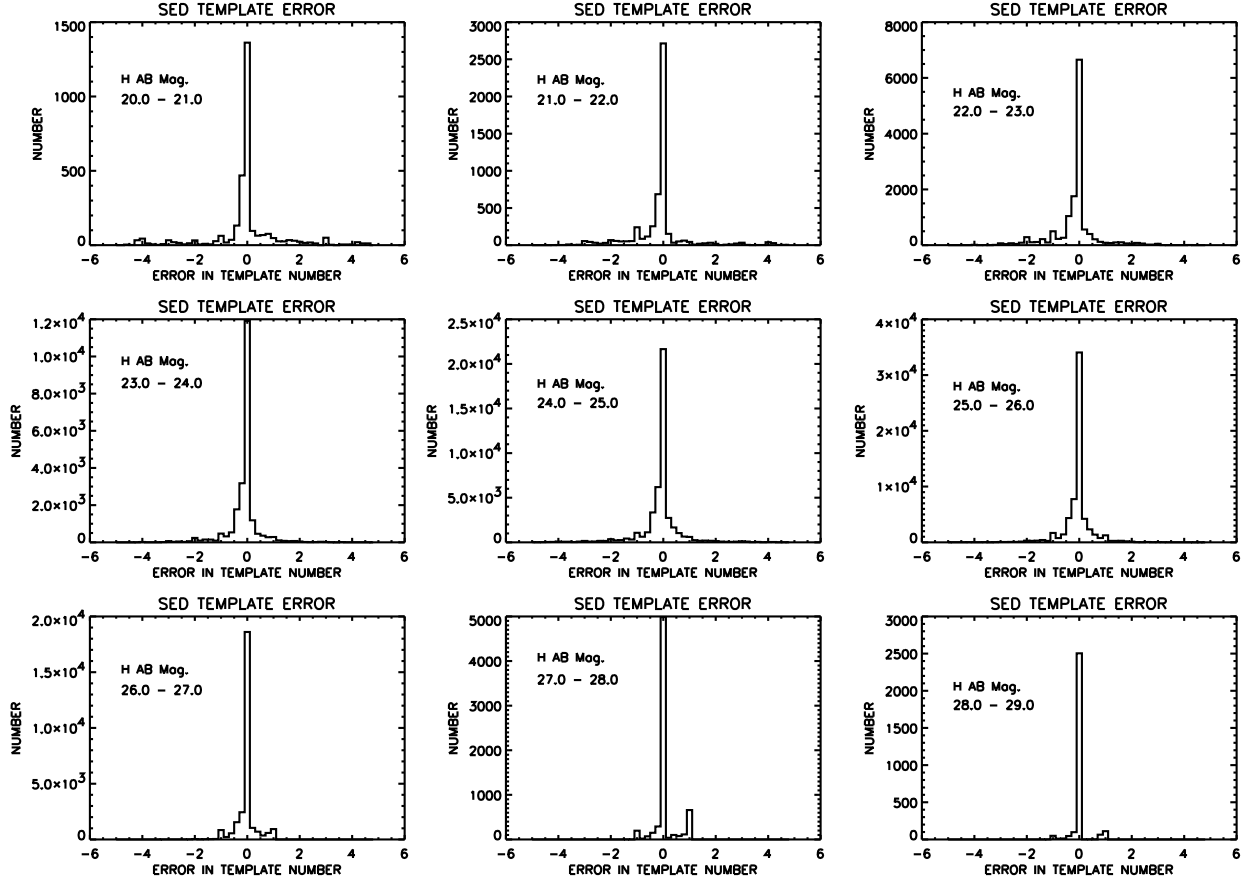


Fig. 13.— The template number error histograms for all sources in Table 2. Negative values indicate that the unperturbed template SED is later than the perturbed SED. Template numbers run from 1, the earliest, to 6, the latest in increments of 0.1

L. Then the expression for I_2 has the form

$$I_2 \simeq C(\gamma) \times (r_o/D)^\gamma \times (D/L) \quad (7)$$

The quantity L/D is simply the number of cubes of dimension $D \times D \times D$ that can be placed end to end in the tube of length L . The dimensionless coefficient $C(\gamma)$ is a double integral in which dV_1 is taken over the unit cube and dV_2 covers that same cube plus a large number of cubes on either side of this unit cube. We have evaluated this coefficient numerically which is vastly simplified by the large number of symmetries in this geometry. From the work of Adelberger et al. (1998) we adopt $\gamma = 1.8$ and $r_o = 5h^{-1}$ Mpc and find $C(\gamma = 1.8) = 8.22$. We use the value of D and L for our adopted cosmology appropriate to the center of each bin.

The calculation was made for a square field equal to one WFPC2 chip and then the errors for the three fields were added in quadrature. The larger field and the increased photometric error means that large scale structure is no longer the dominant but still an important error in extrapolating the SFR history in the NHDF to the SFR history of the universe. The dashed error bars in Figures 9 and 10 are the quadrature sum of the photometric and large scale structure errors.

9. Magnitude Functions and Comparisons with Predictions

Ground based K magnitude functions have provided constraints on galaxy formation models, eg. Kauffmann and Charlot (1998). The much deeper F160W magnitude function determined here provides an even more powerful constraint on theoretical models. A great advantage of this function is that is completely independent of models or cosmology. Figure 14 shows the observed F160W magnitude function for the NHDF. The roll off at magnitudes greater than 28 is due to surface brightness dimming and is not a true feature of the magnitude function. In the range of validity, the magnitude functions from the WFPC2 F814W band (Williams et al. 1996) and the NICMOS F160W band are remarkably similar.

Kauffmann and Charlot (1998) proposed two tests to discriminate between hierarchical galaxy formation and pure luminosity evolution (PLE) of galaxies. Both models were constrained to fit the present day K band luminosity function. Since the predictions are for the K band, K band magnitudes were calculated from the observed 1.6 micron flux using the SEDs found by the analysis. Any error in this transformation is very small compared to the differences in the predictions between the hierarchical and PLE models. The first test compares the number density of galaxies versus K magnitude at redshifts of 0.6, 1.0, and 2.0.

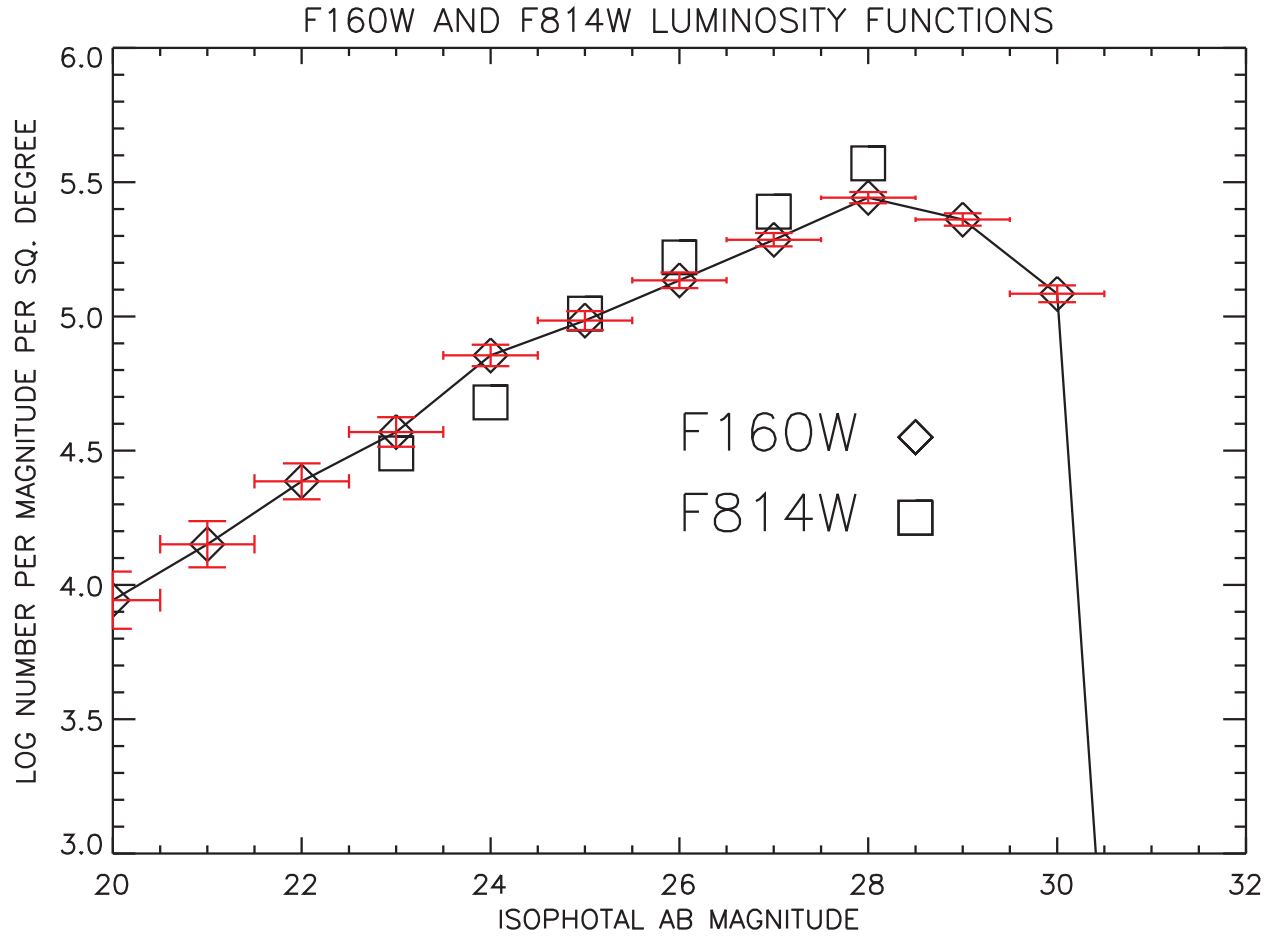


Fig. 14.— The NICMOS F160W (1.6 micron) magnitude function with the WFPC2 0.814 micron magnitude function superimposed.

The PLE model predicts many more bright galaxies at each redshift than do the hierarchical models. Since the predictions only go as faint as a K magnitude of 21.5 the number statistics in the NHDF are small. The PLE model predicts a factor of 10 more bright galaxies than are observed in the NHDF at redshifts of 1 and 2. The hierarchical predictions are within the error bars of the observations.

A more decisive test from Kauffmann and Charlot (1998) is their prediction of the relative fraction of galaxies versus redshift in K magnitude bins. Figure 15 shows the predictions and the observations. The first two magnitude bins have 1 and 0 galaxies in the NHDF but the third K 19-21 bin has a significant number of galaxies. It clearly favors the hierarchical model with the data and prediction being virtually indistinguishable. Although the predictions end at a K magnitude of 21, the data for fainter magnitudes follows an extrapolation of the hierarchical prediction at those magnitudes. The net results of the two tests are consistent with the hierarchical prediction and inconsistent with the PLE prediction.

Our analysis determines the redshift, extinction, and intrinsic SED therefore a combination of the flux, redshift, and SED determines the total luminosity of the galaxy to the accuracy of the individual parameters. The great depth of NHDF observations provides further constraints on galaxy formation models by observing the evolution of the luminosity function with time. Figure 16 shows the luminosity function at 6 different epochs, $z = 1-6$. The roll off of each curve at low luminosities is simply due to galaxies falling below the detection limit. To observational accuracy, the shapes of the luminosity functions at each epoch appear remarkably similar. The low absolute values for the luminosity function at a redshift of 5 may be due to a void in the NHDF at that redshift.

It should be noted that even though the luminosity function appears invariant with redshift to $z = 6$, this does not mean that the mass function is also invariant. Very young galaxies at a redshift of 6 require much less mass to achieve the same luminosity as old, present day galaxies. In fact, the invariant luminosity function appears to favor the hierarchical model of galaxy assembly.

10. Infrared and Sub-mm Constraints

The observed infrared and sub-mm backgrounds place constraints on the extinction values found in our χ^2 analysis. If the extincted luminosity is significantly different from the observed infrared background levels then the extinction values may be considered suspect. A calculated background flux that is much higher than the observed background would indicate an over correction for extinction and a higher SFR than allowed by the infrared and sub-mm

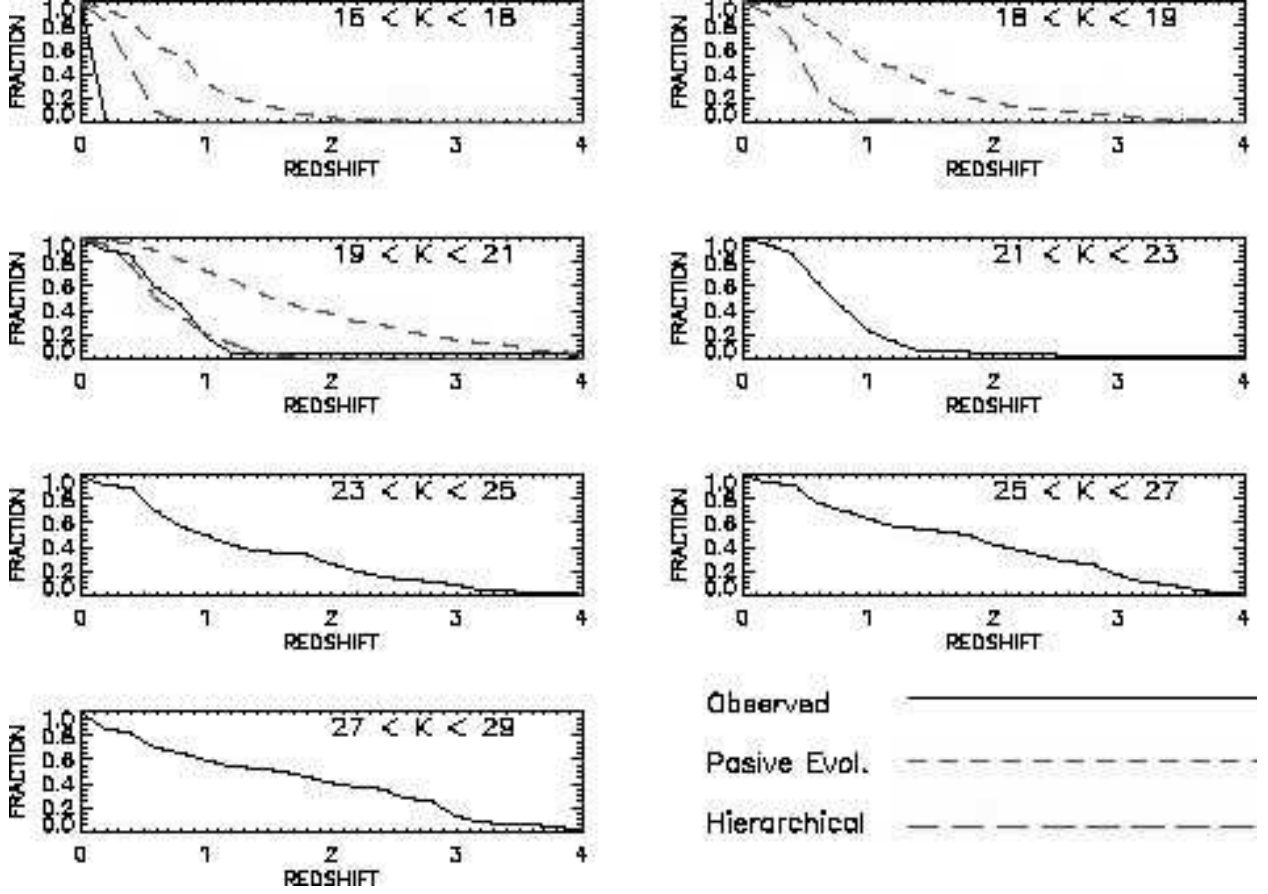


Fig. 15.— Plots of the relative fraction of galaxies with redshifts greater than z in 7 different magnitude bins. Predictions only exist for the first three bins. The first two bins have only 1 and 0 observed galaxies respectively.

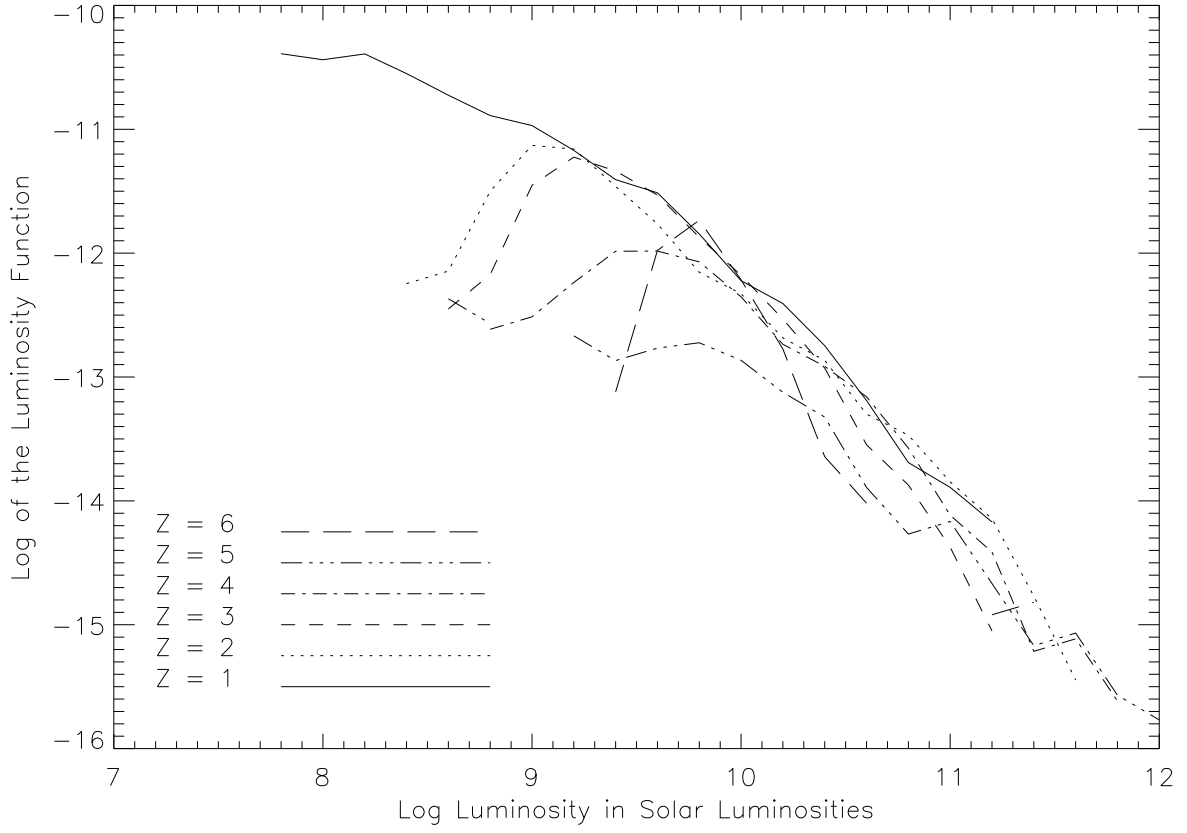


Fig. 16.— The evolution of the 1.6 micron luminosity function with redshift.

constraints. On the other hand, if the extinguished luminosity is much lower than the infrared background levels it would be a sign that our analysis has missed a large part of the highly obscured star formation activity. In addition the calculated sub-mm luminosity of individual sources should not exceed the detections and limits set in the NHDF by Hughes et al. (1998). Note that although comparison with the observed background and emission from individual objects is a constraint on the extinction values, agreement is not a validation of the values. The difference between $E(B-V)$ values of 1 and 2 is a large extinction error but both predict essentially the same amount of re-emitted flux since they both remove almost all of the UV and optical luminosity.

Both Calzetti et al. (2000) and Adelberger and Steidel (2000) have explored the errors in transforming between extinctions derived from the optical flux and the observed infrared emission. Calzetti et al. (2000) estimates that the error is a factor of 2 for individual sources which reduces to 20% for a group of about 50 galaxies. Adelberger and Steidel (2000) cite errors of 0.2 - 0.3 dex (1.6 - 2.0) and ascribe the same range in SFR error. The error bars in Figures 9 and 10 are well within these limits, particularly since the points represent hundreds of galaxies rather than individual galaxies.

10.1. Predicted and Observed Backgrounds

The fraction of luminosity removed by extinction is easily calculated for each SED from the Calzetti obscuration law. This luminosity is assigned to a dust emission SED. Dust SEDs vary significantly (Rigopoulou et al. 1999) but there is no easy way to predict which SED is appropriate from just the optical and near-IR observations. For consistency a single dust SED is used from Figure 1 of Aussel et al. (1999) for the PAH features joined with the Arp 220 ULIRG spectrum given in Figure 4 of Rowan-Robinson and Efstathiou (1993). The SCUBA 850 μm flux as well as the ISO 6 and 15 μm fluxes listed in Table 2 are calculated from the SED, $E(B-V)$, redshift and luminosity.

Integration of all of the predicted 850 μm fluxes gives a 850 μm background of 3.9×10^{-10} watts m^{-2} steradian $^{-1}$. The 850 μm flux is consistent with the value of $5 \pm 2 \times 10^{-10}$ from Blain et al. (1999) and 4×10^{-10} for COBE (Fixsen et al. 1998). The agreement with the probably more accurate COBE flux is remarkable but it should be interpreted only that the predicted sub-mm flux does not indicate an error in the derived parameters

Integration of the observed 1.6 μm fluxes gives a 1.6 μm discrete source background of 7.0×10^{-9} watts m^{-2} steradian $^{-1}$. The previous 1.6 μm background in the Deep NICMOS NHDF from TWS was 6×10^{-9} . The F160W background found here is significantly less

than the J (54×10^{-9}) and K (27.8×10^{-9}) backgrounds found by Cambresy et al. (2001). It is also less than but closer to the K band background of 12.4×10^{-9} found by Wright and Reese (2000). Our background subtraction technique will remove any component of the true background not due to detected discrete sources.

10.2. Individual Sources

Although it is not the primary purpose of the infrared flux calculation, the calculated fluxes of individual sources can be compared with observations and observational limits.

10.2.1. ULIRGs

We define an Ultra Luminous Infrared Galaxy (ULIRG) as a galaxy with greater than $10^{12} L_{\odot}$ total luminosity with half or greater of the luminosity emitted in the mid and far infrared. One of the surprising aspects of TWS was the observation of two ULIRGs in the small $50'' \times 50''$ field of the Deep NICMOS observations. They are sources 439 and 800 in the present catalog. Source 800 retains its ULIRG status in this analysis. Source 800 may also contain an AGN component. Although not listed in their detection catalog, the Chandra X-Ray map of (Brandt et al. 2001b) clearly shows a source at the position of source 800. Source 439 (166 in TWS), however, falls to LIRG status with a luminosity of $1.95 \times 10^{11} L_{\odot}$. The primary reason is that the best fit in this analysis is a template 5.7 and $E(B-V) = 0.5$ fit as compared to a template 5.9 and $E(B-V) = 1.0$ fit in TWS. Although the differences in predicted fluxes is small, the luminosity difference between the two fits is large. Given the higher signal to noise, the parameters found in TWS are more likely correct.

There are two very high redshift galaxies, 22 and 396, with ULIRG level luminosities but their redshifts of 8.0 and 7.44 put them beyond the galaxies considered in this paper. The validity of these source will be left to another study. An additional two candidates included in this analysis are sources 475 and 1364 at redshifts of 6.24 and 4.88 respectively. These do not correspond to any WFPC2 NHDF source and are both outside of the field of the Deep NICMOS image. Source 1364 has a small amount of F814W flux while 475 has no detectable flux in any of the optical bands. Both galaxies have significant F110W and F160W fluxes with very red F160W-F110W colors. The χ^2 plots show two very broad minima at redshifts between 1 and 2 and at the higher redshifts where the fit is the best. Both of the high redshift minima are extremely broad, covering a redshift range of approximately 2 around the selected redshift. Given the nature of the χ^2 distribution, the ULIRG status of these

sources is extremely uncertain.

With no reliable detection of additional ULIRGs in this study we can throw no light on the question of whether ULIRGs were much more prevalent in the past, reaching a peak near a redshift of two. If the two possible ULIRGs above were at a redshift of 2 rather than their high redshifts, their luminosities would be considerably sub-ULIRG. The existence of any ULIRGs in the area of the NHDF is still highly improbable, however, given the local space density of ULIRGs. Resolution of this question will require deep imaging in additional fields.

10.2.2. SCUBA Sources

Probably the most enigmatic sources in the NHDF are the sub-mm sources detected by SCUBA (Hughes et al. 1998). Of the 5 detected HDF sources, source 2 actually lies just outside of the NHDF field and source 3 is in the PC chip which was not analyzed in this work. The remaining sources 1, 4, and 5 are discussed below.

VLA observations by Downes et al. (1999) indicate that the galaxy corresponding to HDF850.1 is either WFPC2 3-586 or 3-593 if it is associated with an optically visible galaxy. It could also be an optically obscured galaxy lying between the two galaxies. Examination of the F160W image does not reveal an optically undetected galaxy lying between the sources, however, the images of the two galaxies slightly overlap at a level below the threshold set for positive detection in § 3. WFPC2 3-586 corresponds to source 1247 in Table 2. It is an elliptical galaxy (Template 1.2) with no detected extinction at a redshift of 0.88. The luminosity is $1.5 \times 10^{10} L_{\odot}$ and it is an unlikely candidate for HDF850.1.

WFPC2 3-593.0 and 3-593.2 correspond to source 1212 in Table 2. This is a very late galaxy (Template 6.0) with an E(B-V) of 0.4 at a redshift of 1.84. It has a luminosity of 1.76×10^{11} but the predicted 850 μm flux is only 0.16 mJy, below the detected flux of 7 mJy. This is a case where the available parameter space of the analysis may have been inadequate to identify this object as the SCUBA source. The analysis picked the hottest SED with a relatively high E(B-V). If an even hotter SED were available it might have given a better fit with a correspondingly higher E(B-V). The combination of the hotter SED and higher E(B-V) could dramatically increase the expected 850 μm flux. Of the two visible sources 3-593 (1212) is by far the better candidate for HDF850.1.

An alternative source is 1277 which lies closer than $1''$ to the position of HDF850.1 given by Hughes et al. (1998). It is barely visible in the F814W band but is a strong source in the F110W and F160W bands. It is a high redshift object ($z = 4.8$) with a extinction of E(B-V)

= 0.3 and a very late template of 5.9. Source 1277 has a luminosity of $1.49 \times 10^{11} L_{\odot}$ and a predicted 850 μm flux of 0.125 mJy which is also below the observed flux. The location of the VLA source however makes this identification much less likely.

Dunlop et al. (2002) have proposed an identification of HDF850.1 as a source located between 3-586.0 and 3-593.1 that is only visible after subtraction of 3-586 in ground based K band images. They also quote a possible detection after subtraction in the F160W images used here. In this scenario the flux of the sub-mm source is lensed with an amplification factor of 3. If this is the true source, it has been missed in the analysis performed here and would only be visible through special processing which is beyond the scope of this paper.

HDF850.4 and HDF850.5 lie very close to each other with a separation of about $12''$. The sources are in fact blended and must be deconvolved (Serjeant et al. 2002). The only nearby source with strong calculated 850 μm flux is source 1108 which lies almost midway between the sources. Its calculated 850 μm flux is 1.36 mJy close to the observed fluxes of 2.3 mJy and 2.1 mJy for HDF850.4 and HDF850.5. The source has a spectroscopic redshift of 0.19, an $E(B-V)$ of 0.6 and a luminosity of $1.55 \times 10^{11} L_{\odot}$. If the shift in position for HDF850.1 to lie on top of 3-593 is applied to HDF850.4 and HDF850.5, HDF850.5 would be within $4''$ of 1108. In this case sources 896 and 905 could be identified with HDF850.4. Their combined predicted flux is equal to 0.89 mJy which is near to the observed flux of 2.3 mJy for HDF850.4.

If the stated detection limit of 2 mJy is taken for the SCUBA observations in the NHDF (Hughes et al. 1998) there is one source in Table 2 that has a predicted 850 μm flux above the limit but was not detected by the SCUBA observations. The source is the ULIRG, source 800, discussed in § 10.2.1. It corresponds to source 277.211 in TWS where its flux was predicted to be 1.5 mJy rather the 3.46 mJy found here. The present analysis found the same redshift, $E(B-V)$ and template as TWS, but the observed F110W and F160W magnitudes were brighter. If the ULIRG contains a AGN component, as is indicated by the x-ray component, the variation might be real but is of surprising magnitude.

VLA 3651+1221

Downes et al. (1999) observed a second source, VLA 3651+1221, very near the elliptical galaxy 3-659.1 which is source 1193 in Table 2. The F160W image shown in Figure 17 clearly shows a strong source at the position of the VLA detection that is very faint or absent in the F814W image. It is clearly a very red source. The correspondence was first noticed by Dickinson et al (2000) who claim that this is the second reddest source in the NHDF. Papovich, Dickinson and Ferguson (2001) point out that the object is also an x-ray source

(Hornschemeier et al. 2000; Brandt et al. 2001a) and therefore probably an AGN. The SE source extraction program linked the source with the elliptical galaxy in producing Table 2, which resulted in an identification of a very late galaxy with a high extinction. This is clearly an artifact of the superposition of fluxes from two very different types of galaxies.

11. Concordance of Star Formation Rates

There has been significant debate (Barger et al. 2000; Blain et al. 1999) on whether optically based studies miss the majority of the star formation in the universe because it is hidden in highly obscured galaxies. The SFRs in Figure 9 for the optical, optical plus near infrared, and submillimeter, however, are all in agreement. On the face of it this would seem to indicate that there is no large missing component of star formation. On the other hand the agreement may be fortuitous or the definitions may be misleading. This section examines the various studies to see what is missing and how the agreement has been achieved.

The only inconsistent measurements in Figure 9 are the measurements of Madau (1999) which show a fall off of star formation at a redshift of 4 and generally lower SFR at all redshifts. The SFRs in Madau (1999) are derived from the numbers presented in Madau, Pozzetti & Dickinson (1998), (note erroneous reference in Madau (1999)) which do not appear to be corrected for surface brightness dimming. The lack of dimming correction appears to be the principal reason for the fall off at high redshifts. The average extinction correction in Madau (1999) is $A_{1500} = 1.2$, which is an underestimate according to this work and accounts for the lower values at redshifts 1 to 2.

The extinction corrected SFRs at redshifts 3 and 4 from Steidel et al. (1999), corrected for the cosmology adopted here, are coincident with the SFRs found in this work. The extinction corrected values were found by multiplying the uncorrected SFRs by 4.7, corresponding to an $E(B-V) = 0.15$ (Steidel et al. 1999). The extinction correction value in Steidel et al. (1999) is well motivated and is interpreted there as the proper correction to the UV flux from observed galaxies in the study. It could also be interpreted as a lower $E(B-V)$ correction to the observed galaxies plus a factor that accounts for galaxies not observed due to very high extinction. Without determining an extinction for each galaxy in the sample it is not possible to separate the two interpretations. It still leaves the possibility that the actual average extinction to the observed galaxies is less than $E(B-V) = 0.15$ and that there are other undetected galaxies that contribute to the SFRs observed by Barger et al. (2000). Note that the comparison with the Steidel et al. (1999) in Barger et al. (2000) Figure 11 is to the uncorrected rate and a $\Lambda = 0$ universe.

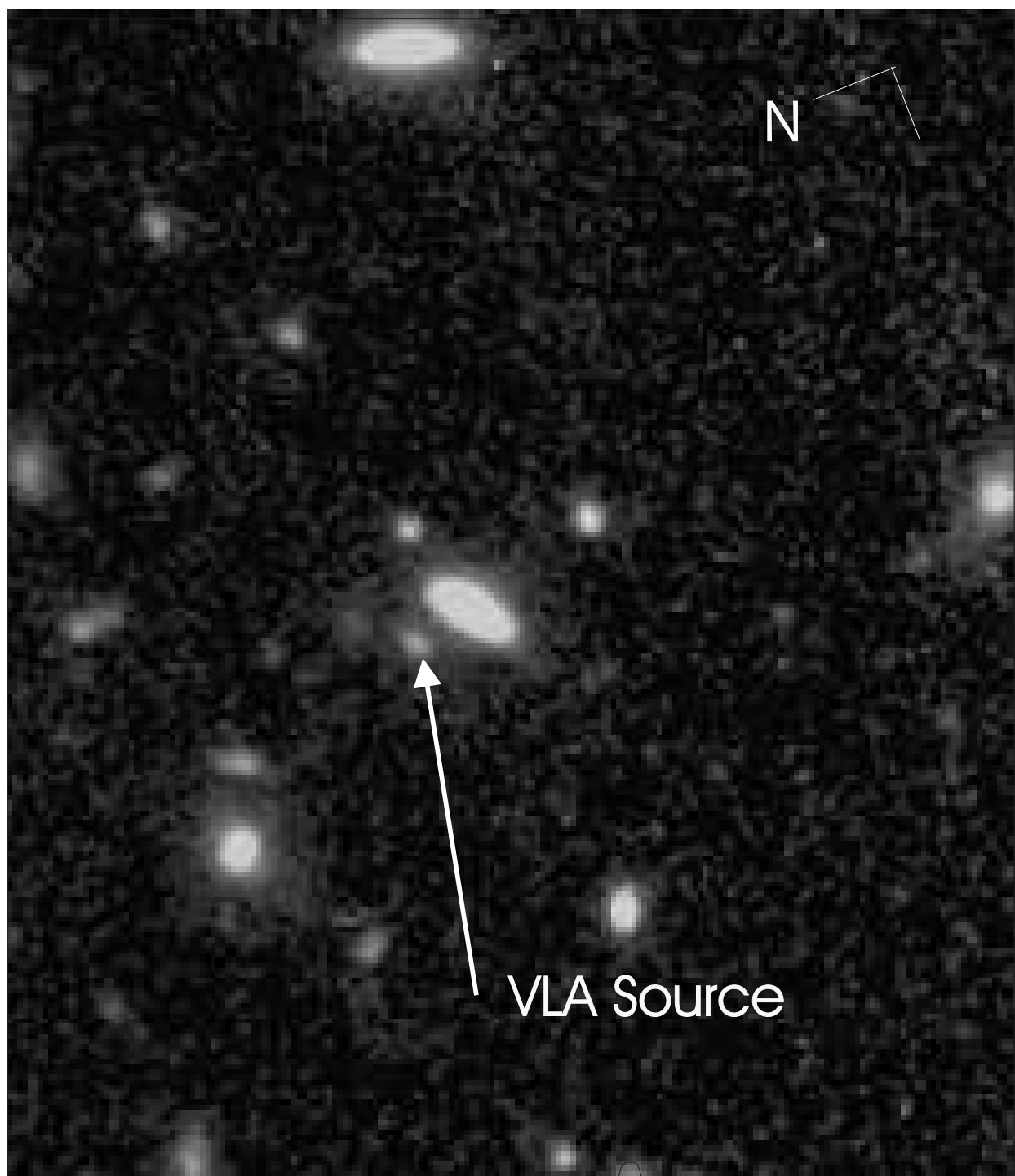


Fig. 17.— The extremely red object associated with VLA 3651+1221.

The SFRs in this work are both extinction corrected on an individual galaxy basis and corrected for surface brightness dimming. The extinction correction at redshifts 2 and 4 are 4.9 and 6.1, near the range of the Steidel et al. (1999) correction. The surface brightness dimming corrections are 2.0 in both cases, therefore, the extinction correction is the dominant correction rather than galaxies or parts of galaxies undetected due to surface brightness dimming. This would appear to indicate that the observed sub-mm SFR can be accounted for by galaxies that are observable in deep HST optical and near infrared observations if not necessarily optical ground based observations.

It can also be argued that the present work has been unsuccessful in identifying the 3 observed sub-mm sources in the fields of the 3 WF chips. There is no doubt that there can be luminous galaxies that are so highly extinguished that even deep HST observations will miss them. At a redshift of 3 the F160W NICMOS band is measuring the 4000 Å flux which can be severely extinguished. It is also possible that the optical depth that can be reached with the F160W filter is less than the total optical depth of the galaxy so that the present analysis determines a lower luminosity and extinction than is actually present in the galaxy. Another possibility is that the assumed dust SED is not appropriate for the bright sub-mm sources. The luminosity in the 850 μ m SCUBA band is a small fraction of the total dust luminosity, therefore, small changes in the dust SED can greatly change the 850 μ m luminosity without significantly affecting the total dust luminosity. Perhaps the bright sub-mm sources have colder dust SEDs than the Arp 220 dust SED used here. The bottom line is that on an individual source level there are many uncertainties that can lead to erroneous sub-mm predictions in the present analysis. It should be noted, however, that the sub-mm predictions are only intended to serve as a check on the total sub-mm power not as a individual source predictor.

In assessing the effect of underpredicting the bright sub-mm sources it should be noted that the correction factor used in Barger et al. (2000) to account for the fainter undetected sources is a factor of 11, therefore, the bright sub-mm sources account for less than 10% of the SFR. Based on the size of the correction it might be argued that the majority of star formation is also missed by the sub-mm observations. The correction to the sub-mm observations depends on the assumed luminosity function whereas the correction to the optical and near IR observations depends on the assumed extinction law. Even if all of the observed sub-mm sources are missed by optical and near-IR studies, the error in the SFR is small. It can be argued that at the depth of the HST observations only the most obscured sources are missed and that the bulk of the galaxies that produce the sub-mm emission and the majority of the SFR are detected and on the average properly accounted for. Within the caveats discussed above it appears that although some of the extreme sub-mm sources are missed by the optical and near infrared observations, the total SFR derived from optical,

optical and near infrared, and sub-mm observations are in agreement indicating that the majority of the SFR is accounted for in the three types of observations. All of these methods however, have correction factors on the order of a factor of 10 based on assumptions that still need to be confirmed.

12. Summary

Analysis of HST archival data from WFPC2 and NICMOS in the NHDF yields photometric redshifts, extinctions and SEDs for almost 2000 galaxies. From this data the extinction corrected SFR for each galaxy was determined. After correction for surface brightness dimming and the variable sensitivity over the NICMOS detector arrays, the star formation history of the NHDF from a redshift 1 to 6 shows a roughly constant SFR. Optical studies of Lyman break galaxies and sub-mm observations produce SFRs that are consistent with the results in this study. The sub-mm background predicted from our analysis is consistent with the observed background, indicating that the analysis has not missed a significant star forming component due to high extinction. The inability to accurately predict the fluxes and locations of the observed NHDF sub-mm sources does indicate that some bright sub-mm sources are certainly missed by this work but that these are not the sources that contribute the majority of star formation in the field.

13. Acknowledgements

The author would like to acknowledge the significant contributions to this work by Ray Weymann and Lisa Storrie-Lombardi in the initial data reduction and analysis as well as their contributions in establishing the methodology which was carried over from TWS. The author would also like to thank Mark Dickinson and all of his group who planned and executed the NICMOS observations of the entire Northern HDF in a General Observer program. This work is supported in part by NASA grant NAG 5-10843. This article is based on observations with the NASA/ESA Hubble Space Telescope, obtained at the Space Telescope Science Institute, which is operated by the Association of Universities for Research in Astronomy under NASA contract NAS5-26555.

REFERENCES

- Adelberger, K. L., Steidel, C. C., Giavalisco, M., Dickinson, M., Pettini, M., & Kellogg, M. 1998, *ApJ*, 505, 18
- Adelberger, K. L. & Steidel, C. C. 2000, *ApJ*, 544, 218
- Aussel, H., et al. 1999, *Å*, 342, 313
- Barger, A.J., Cowie, L.L., & Richards, E.A. 2000, *AJ*, 119, 2092
- Bertin, E., & Arnouts, S. 1996, *A&A*, 117, 393
- Blain et al. 1999, *ApJ*, 512, L87
- Brandt, W. M., et al. 2001, *AJ*, 112, 1
- Brandt, W. M., et al. 2000, *AJ*, 122, 2801
- Bruzual, G. and Charlot, S. 1996, *GISSEL96*
- Calzetti, D., Kinney, A. L., & Storchi-Bergmann, T. 1994, *ApJ*, 429, 582
- Calzetti, D. 1999 Private communication of digital data.
- Calzetti, D. 1997, *AJ*, 113, 162
- Calzetti, D., Armus, L., Bohlin, R.C., Kinney, A.L., Koornneef, J., & Storchi-Bergmann, T. 1999, *ApJ*, 533, 682
- Calzetti et al. 2000, *ApJ*, 533, 682
- Cambresy, L. et al. 2001, *ApJ*, 555, 563
- Cohen, J.G., Hogg, D.W., Blandford, R., Cowie, L.L., Hu, E., Songaila, A., Shopbell, P., & Richberg, K. 2000, *ApJ*, 538, 29
- Cohen, J.G. 2001, *AJ*, 121, 2895
- Coleman, G.D., Wu, C-C, & Weedman, D.W., 1980 *ApJS*, 43, 393
- Dickinson, M. 2000, *Phil.Trans. Royal Soc. Lond. A.*, 358, 2001
- Dickinson M. et al. 2000, *ApJ*, 531, 624
- Downes, D. et al. 1999, *A&A*, 347, 809

- Dunlop, J. S. et al. 2002, astro-ph/0205489
- Fernández-Soto, A., Lanzetta, K.M., & Yahil, A. 1999, ApJ, 513, 34
- Fixsen et al. 1998, ApJ, 508, 123
- Hopkins, A. M., Connolly, A.J., & Szalay, A. S. 2000, AJ, 120, 2843
- Hornschemeier, A. E., et al. 2000, ApJ, 541, 49
- Hughes, D., et al. 1998, Nature, 394, 241
- Kauffmann, G. & Charlot, S. 1998, MNRAS, 297, L23
- Lanzetta, K.M., Yahata, N., Pascarelle, S., Chen, H.-W. & Fernández-Soto, A. 2002, ApJ, 570, 492
- Lanzetta, K.M., Chen, H-W., Fernandez-Soto, A., Pascarelle, S., Puetter, R., Yahata, N., and Yahil, A. 1999, ASP Conf. Ser. 191, Photometric Redshifts and High Redshift Galaxies, ed. R. J. Weymann, L.J. Storrie-Lombardi, M. Sawicki, and R. J. Brunner, (San Francisco ASP), 223.
- Lanzetta, K.M., Yahil, A., & Fernández-Soto, A. 1996, Nature, 381, 759
- Lilly, S. J., Le Fèvre O., Hammer, F., & Crampton, D. 1996, ApJ, 460, L1
- Lytle, D., Stobie, E., Ferro, A. & Barg, I. 1999, in ASP Conf. Ser. 172, Astronomical Data Analysis Software and Systems VIII, ed. D. Mehringer, R. Plante, & D. Roberts, (San Francisco; ASP), 445
- Madau, P., Ferguson, H.C., Dickinson, M. E., Giavalisco, M., Steidel, C. C. & Fruchter, A. 1996, MNRAS, 283, 1388
- Madau, P., Pozzetti, L., & Dickinson, M. 1998, ApJ, 498, 106
- Madau, P. 1999, AIP Conference Proceedings 470, After the Dark Ages: When Galaxies were Young (The Universe at $2 < z < 5$), ed. Stephen S. Holt & Eric P. Smith, (Woodbury, New York AIP), 299
- Papovich, C., Dickinson, M. & Ferguson, H. C. 2001, ApJ, 559, 620
- Peebles, P.J.E. 1980 The Large Scale Structure of the Universe, Princeton University Press, Princeton New Jersey
- Rigopoulou, D., et al. 1999, AJ, 118, 2645

- Rowan-Robinson, M., & Efstathiou, A. 1993, MNRAS, 263, 675
- Serjeant, S. et al. 2002, astro-ph/0201502
- Steidel, C. C., Adelberger, K. L., Giavalisco, M., Dickinson, M., & Pettini, M. 1999, ApJ, 519, 1
- Szalay, A.S., Connolly, A.J., & Szokoly, G.P. 1999, AJ, 117, 68
- Thompson et al. 1999, AJ, 117, 7
- Thompson, R.I., Weymann, R.J. & Storrie-Lombardi, L.J. 2001, ApJ, 546, 694 (TWS)
- Thompson, R. I., ApJ, 581, L85
- Wang, Y., Bachall, N., & Turner, E.L. 1998, AJ, 116, 2081
- Williams, R.E. et al. 1996, AJ, 112, 1335
- Wright, E.L. & Reese, E.D. 2000, ApJ, 545, 43
- Yan, L., McCarthy, P.J., Freudling, W., Teplitz, H.I., Malumuth, E.M., Weymann, R. J., & Malkan, M.A. 1999, ApJ, 519, L47

Table 1. Galaxies with Redshift Errors Greater than 0.5.

ID	WFPC-ID	Phot. Z	Spec. z	Template	E(B-V)	Qual. ^a	Sp. ^b	fail ^c
6	4-916	0.08	0.904	6.0	0.6	9	A	P
13	4-928	0.48	1.015	6.0	1.0	4	E	P
84	4-878	0.0	0.892	3.0	0.04	4	E	S,P
108	...	1.84	0.584	5.2	0.5	3	A	S
339	4-445	1.84	2.5	5.8	0.3	2	EA	S
369	...	1.92	2.801	5.9	0.3	3	A	...
524	2-251	0.24	0.962	4.3	0.4	6	Q	...
625	2-201	1.84	1.313	5.0	0	1	E	S,P
1226	2-531	0.56	1.087	5.8	0.5	3	A	F,P
1656	2-982	0.56	1.147	5.7	0.4	1	E	F
1762	...	1.12	0.47	3.5	0.0	1	E	P

^aThis is the quality of the spectrum as noted in Cohen et al. (2000) where 1 is the highest 11 is the lowest cited in table 2b of that work.

^bSp is the spectral type listed in Cohen et al. (2000). E is an emission line galaxy, A is an absorption line galaxy, EA is a galaxy displaying both emission and absorption and Q is a broad absorption line galaxy

^cFail is the probable cause of failure. P is hitting a boundary in parameter space, S is the probable superposition of two galaxies, and F is the problem associated with $z = 0.56$ discussed in the text.

The remainder of the 1927 table entries are available in the electronic version of the *Astrophysical Journal* publication.

Table 2. Listing of measured quantities

NICMOS ID	WFPC ID	z	E(B-V)	SFR M_{\odot} yr^{-1}	Lum. L_{\odot}	frac. ^a	ISO6 6 μm flux mJy	ISO15 15 μm flux mJy	SCUBA 850 μm flux mJy	T ^b	χ^2	Tot. ^c mag	Ap. ^d mag	RA 12 ^h 36 ^m	DEC +62 ^o
1	4-951.0	0.00	0.50	2.831	0.00E+00	0.86	0.00E+00	0.00E+00	0.00E+00	5.6	3.0	26.4	27.4	38.23	12:28.3
2	...	2.88	0.00	0.258	3.64E+09	0.00	0.00E+00	0.00E+00	0.00E+00	3.5	18.	28.2	27.2	38.24	12:31.7
3	...	2.56	0.00	0.131	2.15E+09	0.00	0.00E+00	0.00E+00	0.00E+00	3.3	19.	28.2	27.3	38.32	12:34.2
4	...	2.56	0.10	0.691	3.94E+09	0.39	5.16E-06	7.82E-06	1.61E-03	5.1	5.6	28.7	27.2	38.32	12:32.2
5	...	2.80	0.00	1.984	7.36E+09	0.00	0.00E+00	0.00E+00	0.00E+00	5.8	19.	27.1	27.1	38.49	12:35.5
6	4-916.0	0.90	0.60	0.182	6.34E+08	0.95	1.90E-05	1.61E-04	8.75E-04	6.0	11.	22.5	24.6	38.59	12:33.8
7	4-922.0	3.20	0.20	2.937	1.18E+10	0.53	0.00E+00	2.10E-05	6.76E-03	5.6	2.6	27.8	27.7	38.60	12:29.1
8	4-952.0	3.52	0.20	5.092	2.15E+10	0.51	0.00E+00	3.00E-05	1.29E-02	5.5	4.6	27.4	27.3	38.77	12:18.8
9	4-930.0	0.48	0.30	0.662	2.46E+09	0.75	2.63E-04	1.76E-03	4.70E-03	5.8	8.1	24.2	25.7	38.79	12:25.9
10	4-953.0	2.88	0.00	0.587	2.62E+09	0.00	0.00E+00	0.00E+00	0.00E+00	5.4	2.2	27.5	27.9	38.83	12:17.9

^aThis is the fraction of the luminosity removed by extinction and re-emitted in the mid and far infrared

^bThe selected template number between 1.0 (early-cold) and 6.0 (late-hot).

^cThe total AB magnitude in the F160W filter.

^dThe F160W magnitude in an 0.6'' diameter aperture.

Table 3. Properties of galaxies with F160W magnitudes significantly brighter than predicted L* magnitudes.

ID	WFPC-ID	Redshift	F160W AB mag.	E(B-V)	Template	Lum.
1636.0	3-839.0	5.2	23.8	0.02	5.1	5.72E11
398.0	4-555.11	3.04	24.4	0.08	5.6	2.7E11
410.0	4-555.1	2.799	23.8	0.20	5.7	6.09E11
81.0	4-713	4.08	23.6	0.00	3.9	4.96E11
1604.0	3-82	4.32	24.3	0.10	3.6	6.5E11
1630.0	3-367	4.48	24.8	0.06	3.5	3.66E11
1409.0	2-591	2.96	24.4	0.00	5.2	8.84E10
1179.0	2-578	3.92	25.0	0.00	5.2	1.09E11
812.0	4-169	5.04	25.2	0.10	3.9	3.38E11

Table 4. SFR corrections for extinction and surface brightness dimming

z	Uncor. SFR	Ext. Cor. SFR	Ext.& Dim. Cor. SFR	% Lum. ^a Missing
1	6.8E-3	2.8E-1	2.8E-1	0%
2	3.7E-2	1.8E-1	3.7E-1	50%
3	5.0E-2	8.9E-2	9.6E-2	8%
4	1.0E-1	6.1E-1	1.2E-1	50%
5	1.8E-2	6.5E-2	2.3E-1	72%
6	3.5E-2	8.1E-2	3.0E-1	73%

^aThis is the percentage of missed luminosity between the extinction corrected SFR and the extinction corrected SFR also corrected for surface brightness dimming.

Table 5. Sources of Numerical Variances

Statistic	$z = 1$	$z = 2$	$z = 3$	$z = 4$	$z = 5$	$z = 6$
Number of Sources	495	370	339	160	45	55
$1/\sqrt{N}$	0.045	0.052	0.058	0.079	0.15	0.13
I_2	0.16	0.11	0.13	0.16	0.19	0.21
σ_N/N	0.09	0.11	0.13	0.16	0.19	0.21
16% Confidence fraction	0.47	0.48	0.21	0.27	0.64	0.82
84% Confidence fraction	0.37	0.21	0.69	1.2	1.1	0.13